SAPIENZA
UNIVERSITÀ DI ROMA

Facoltà di Scienze Matematiche Fisiche e Naturali

Corso di laurea in Fisica
Anno Accademico 2011-2012

Tesi di Laurea Magistrale

Effects of Two-Body Currents on the Nuclear Electroweak response

Relatore:
Prof. Omar Benhar Noccioli

Candidata:
Noemi Rocco

Contents

Introduction

Experimental searches of neutrino oscillations exploit neutrino-nucleus interactions to detect the beam particles, the properties of which are largely unknown. The use of nuclear targets as detectors, while allowing for a substantial increase of the event rate, involves non trivial problems, as the interpretation of the observed signal requires a quantitative understanding of neutrino-nucleus interactions. Given the present experimental accuracy, the treatment of nuclear effect is in fact regarded as one of the main sources of systematic uncertainty (see, e.g., Ref.[1]).

Over the past decade, a growing effort has been made, aimed at making use of the knowledge acquired from experimental and theoretical studies of electron-nucleus scattering.

Electron-nucleus scattering cross sections are usually analyzed at fixed beam energy E_e, and electron scattering angle θ_e as a function of the energy loss ω. As an example, Fig.1 shows the typical behavior of the double differential cross sections of the inclusive process

$$e + A \to e' + X \ , \tag{1}$$

in which only the outgoing lepton is detected, at beam energy around 1 GeV. Here, A and X denote the target nucleus and the undetected final hadronic state, respectively.

It is apparent that the different reaction mechanisms, yielding the dominant contributions to the cross section at different values of ω (corresponding to different values of the Bjorken scaling variable $x = Q^2/2M\omega$, where M is the nucleon mass and

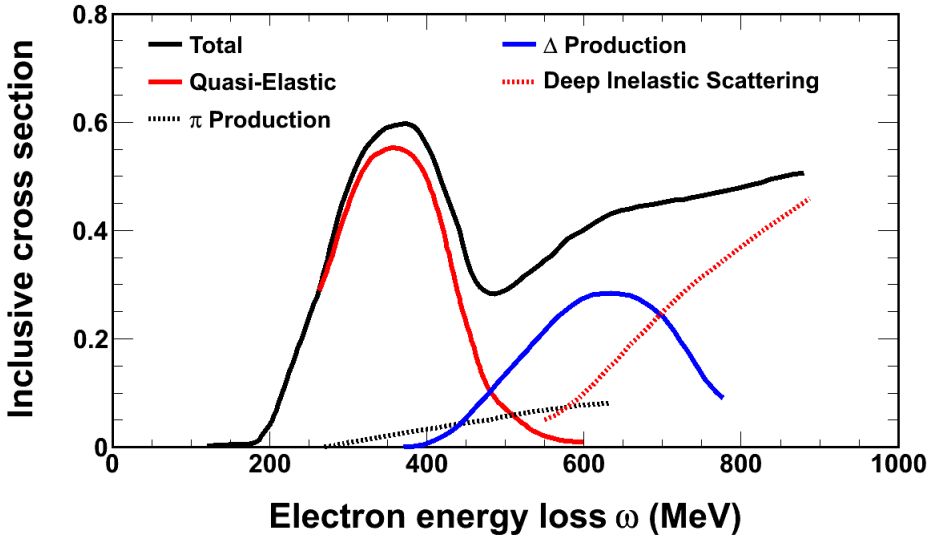

Figure 1: Schematic representation of inclusive electron-nucleus cross section as a function of energy loss.

$Q^2 = 4E_e(E_e - \omega)\sin^2\theta_e/2)$ can be easily identified.

The bump centered at $\omega \sim Q^2/2M$, or $x \sim 1$, the position and width of which are determined by the momentum and removal energy distribution of the struck particle, corresponds to the single nucleon knockout, while the structure visible at larger ω reflects the onset of coupling to two-nucleon currents, arising from meson exchange processes, excitation of nucleon resonances and deep inelastic scattering.

The available theoretical models of electron-nucleus scattering provide an overall satisfactory description of the data over a broad kinematical range. In particular, in the region in which quasi elastic scattering dominates, the data is reproduced with an accuracy of few percent (for a recent review on electron-nucleus scattering in the quasi elastic sector, see Ref. [2]).

In neutrino experiments, the beam energy is *not* known and the detection of the particles in the final state *does not* provide a measurement of the energy transfer, ω. As a

consequence, the contributions of the different reaction mechanisms, which in Fig. 1 can be easily identified, mix up, thus hindering the interpretation of the data.

The difficulties associated with the description of the neutrino-nucleus cross section have recently emerged in the analysis of the data set of charged-current quasi elastic (CCQE) events released by MiniBooNE collaboration [9]. Theoretical models providing a quantitative account of the electron-nucleus cross section in the kinematical region in which quasi elastic scattering dominates fail to explain the large excess of measured CCQE events [10]. It has been argued that this failure is likely to be ascribed to the contribution of reactions mechanisms other than single nucleon knock out, leading to two particle-two hole final states [10, 11, 12].

In this Thesis, we discuss the preliminary results of a study of one of these mechanisms, namely processes involving two-body currents arising from meson-exchange.

As a first step, our analysis has been restricted to the pion-exchange contribution to the electron scattering cross section. Moreover, to keep the formalism as simple as possible, we have considered the case of a deuterium target.

The Thesis is structured as follows.

Chapter 1 is devoted to a summary of neutrino Physics. After introducing both the Majorana and Dirac definitions of the ν-field, we discuss how two- and three-neutrino mixing lead to neutrino oscillations, and provide a brief description of the experiments designed to detect them.

In Chapter 2, we focus on the somewhat controversial results reported by the MiniBooNE experiment, and discuss the so called axial mass puzzle, as well as its possible explanations. The formalism employed to obtain the neutrino-nucleus cross section in the impulse approximation (IA) regime is described in Chapter 3. We will show that under the assumptions underlying IA, which are expected to be justified at neutrino energies $\gtrsim 1$ GeV, the nuclear cross section can be written in terms of the target spectral function

and the elementary neutrino-nucleon cross section.

In Chapter 4, we confront electron and neutrino scattering experiments, and highlight the difficulties arising from flux average.

The derivation of the nuclear cross section including one- and two-body current is discussed in Chapter 5 in the case of electromagnetic current and deuterium target. Preliminary results of numerical calculations are also reported.

In Chapter 5 is devoted to the discussion of meson-exchange-currents and their contribution to the nuclear cross sections. After describing a preliminary study on electromagnetic currents and pion exchange,we will eventually derive the expression of the nuclear cross section including one- and two- body currents.

Finally, in the concluding Section we summarize our findings and state the conclusions.

Chapter 1

Neutrino masses and oscillations

It has long been known that neutrinos are very light. However, determining whether they are truly massless or have small but nonzero masses turned out to be a severe experimental challenge.

Recently, strong evidence that neutrinos do have nonzero masses has at long emerged. This evidence stems from the observation that a neutrino of one type, or *flavor*, such as a muon neutrino, can turn into a neutrino of a different flavor, such as a tau neutrino. This metamorphose, known as neutrino oscillation, besides necessarily implying non vanishing neutrino masses, also suggests that neutrinos may be Majorana particles, and that lepton number may not be conserved.

In this Chapter, after discussing the nature of the neutrino mass, we will briefly review the physics of neutrino oscillations and their experimental search.

1.1 Neutrino mass

1.1.1 Dirac mass term

The Standard Model of Particle Physics is based on spontaneous symmetry breaking and the Higgs mechanism, providing the masses of charged leptons. Applying the same

scheme to neutrinos leads to the appearance of a mass term of the form

$$\mathcal{L}_D = -m_D\bar{\nu}\nu = -m_D(\bar{\nu}_L\nu_R + \bar{\nu}_R\nu_L) = -\frac{yv}{\sqrt{2}}(\bar{\nu}_L\nu_R + \bar{\nu}_R\nu_L) \tag{1.1}$$

in the lagrangian density. In the above equation, m_D is the Dirac neutrino mass, y is the Yukawa coupling and v is the vacuum expectation value of the Higgs field.

Note that, in addition to the left-handed component of the neutrino field, ν_L, the Dirac mass term of Eq.(1.1) involves the right-handed component, ν_R, which has not been observed. Moreover, the Higgs mechanism generates a neutrino mass of the same order of the mass of the associated charged lepton, and does not provide an explanation of the huge difference resulting from experimental measurements.

1.1.2 Majorana mass term

In his celebrated 1937 paper [3], Majorana observed that a neutral massive fermion can be described by a two-component spinor field ψ such that

$$\psi = \psi^C = \mathcal{C}(\gamma^0)^T\psi^* \ , \tag{1.2}$$

where $\mathcal{C}$ is the charge conjugation operator, satisfying the relations $\mathcal{C}(\gamma^\mu)^T\mathcal{C}^{-1} = -\gamma^\mu$, $\mathcal{C}^\dagger = \mathcal{C}^{-1}$ and $\mathcal{C}^T = -\mathcal{C}$.

The action of the projection operator $P_L = (1-\gamma_5)/2$ on the field ψ leads to:

$$P_L\psi = \psi_L = \psi_R^C \ , \tag{1.3}$$

providing a relation between the right- and left- handed components of the Majorana neutrino:

$$\psi = \psi_L + \psi_L^C \ . \tag{1.4}$$

From the above equation, it is apparent that the field ψ only depends on the two components of ψ_L.

The Majorana mass term takes the form:

$$\mathcal{L}_M = -\frac{1}{2} m_M (\bar{\psi}_L \psi_R + \bar{\psi}_R \psi_L) = -\frac{1}{2} m_M (\bar{\psi}_R^C \psi_R + \bar{\psi}_L^C \psi_L) \tag{1.5}$$

where the factor 1/2 has been included in order to get the right equations of motion.

1.1.3 Dirac-Majorana mass term

From the above discussion, it follows that the most general expression we can choose to write the mass term appearing in the lagrangian density is

$$\mathcal{L}_{\text{mass}} = \mathcal{L}_D + \mathcal{L}_M^{\text{right}} + \mathcal{L}_M^{\text{left}} \ . \tag{1.6}$$

It can be conveniently rewritten in matrix form as

$$\mathcal{L}_{\text{mass}} = -\frac{1}{2} \bar{N}_L^C M N_L + \text{h.c.} = -\frac{1}{2} (\bar{\nu}_L^C \ \bar{\nu}_R) \begin{pmatrix} m_L & m_D \\ m_D & m_R \end{pmatrix} \begin{pmatrix} \nu_L \\ \nu_R^C \end{pmatrix} + \text{h.c.} \tag{1.7}$$

For $m_D \neq 0$ the above lagrangian does not provide definite values of the masses associated with the fields ν_L e ν_R. In order to identify the mass eigenstate we have to diagonalize the mass matrix M.

Let us introduce the fields ν_1 e ν_2, associated with the neutrino mass eigenstates, and the matrix U diagonalizing M. If M is real, U can be cast in the factorized form

$$U = R(\theta)\rho \ , \tag{1.8}$$

with

$$R(\theta) = \begin{pmatrix} \cos\theta & \sin\theta \\ -\sin\theta & \cos\theta \end{pmatrix}, \quad \rho = \begin{pmatrix} \rho_1 & 0 \\ 0 & \rho_2 \end{pmatrix} \tag{1.9}$$

and $|\rho_k|^2 = 1$.

The matrix R is determined by imposing the condition

$$R^T M R = \begin{pmatrix} m_1' & 0 \\ 0 & m_2' \end{pmatrix} \ , \tag{1.10}$$

yielding

$$\tan 2\theta = \frac{2m_D}{m_R - m_L} \qquad m'_{1,2} = \frac{1}{2}\left[(m_L + m_R) \pm \sqrt{(m_L - m_R)^2 + 4m_D^2}\right] \ . \tag{1.11}$$

Collecting together the above results we finally obtain

$$U^T M U = \rho^T R^T M R \rho = \begin{pmatrix} \rho_1^2 m'_1 & 0 \\ 0 & \rho_2^2 m'_2 \end{pmatrix} \ . \tag{1.12}$$

1.1.4 The see-saw mechanism

The Standard Model of Particles Physics, providing a wealth of predictions in impressive agreement with experiments, can be used to constrain the parameters entering the theory of neutrino mass discussed in the previous Section. The requirement that the neutrino mass term in the lagrangian be invariant under $SU(2)_L$ transformations implies that

- since the left-handed neutrino belongs to a weak isospin doublet with $I_3 = +1/2$, the product $\nu_L \bar{\nu}_L^C$ belongs to a weak isospin triplet, with $I_3 = 1$. Hence $m_L = 0$;
- $m_R \neq 0$ is allowed, as $\bar{\nu}_R^C \nu_R$ transforms as a singlet under $SU(2)_L$;
- there are no restriction on m_D, since the corresponding term is produced by the standard Higgs mechanism.

From the above considerations, it follows that, assuming $m_L = 0$, $M \in \Re$ and $m_D \ll m_R$, we obtain

$$m_1 \approx \frac{m_D^2}{m_R} \ll m_D, \quad m_2 \approx m_R, \quad \tan\theta \approx \frac{m_D}{m_R} \ll 1, \quad \rho_1^2 = -1 \ . \tag{1.13}$$

The see-saw mechanism for the production of neutrino masses is defined by the above equations. It states that a very light ν_1, the mass of which is considerably smaller than the mass of the corresponding charged lepton, is associated with a very heavy ν_2 (m_2 is the same order as m_R).

1.1.5 Three-flavor mass matrix

The diagonalization of the mass matrix in the case of three neutrino flavors can be carried out retracing the steps of the above discussion. Following the same procedure developed to obtain the CKM matrix, describing quark mixing, we diagonalize the mass matrix through the introduction of the neutrino mixing matrix. Let us start writing the left-handed fields in the form

$$N_L = \begin{pmatrix} \nu_L \\ \nu_R^C \end{pmatrix}, \quad \nu_L = \begin{pmatrix} \nu_{eL} \\ \nu_{\mu L} \\ \nu_{\tau L} \end{pmatrix}, \quad \nu_R^C = \begin{pmatrix} \nu_{s_1 R}^C \\ \nu_{s_2 R}^C \\ \nu_{s_3 R}^C \end{pmatrix} , \tag{1.14}$$

leading to

$$\mathcal{L}_{\text{mass}} = \bar{N}_L M N_L = \begin{pmatrix} \bar{\nu}_L & \bar{\nu}_R^C \end{pmatrix} \begin{pmatrix} M_L & M_D^T \\ M_D & M_R \end{pmatrix} \begin{pmatrix} \nu_L \\ \nu_R^C \end{pmatrix} , \tag{1.15}$$

M being a 6×6 matrix. Note that the number of right-handed fields is not restricted, as right-handed neutrino are *sterile*, i.e. not subject to weak interactions, and as such non observable.

Introducing the neutrino mass eigenstates, denoted by ν_k:

$$N_L = V n_L, \quad n_L = \begin{pmatrix} \nu_{1L} \\ \vdots \\ \nu_{6L} \end{pmatrix} , \tag{1.16}$$

where

$$V^T M V = \begin{pmatrix} m_1 & 0 & \dots & 0 \\ 0 & m_2 & \dots & 0 \\ \vdots & \vdots & \ddots & \vdots \\ 0 & 0 & \dots & m_6 \end{pmatrix} , \tag{1.17}$$

we finally get the equations describing neutrino mixing:

$$\nu_{\alpha L} = \sum_{k=1}^{6} V_{\alpha k} \nu_{kL} \ , \ \alpha = e, \mu, \tau \ , \ \nu_{sR}^C = \sum_{k=1}^{6} V_{sk} \nu_{kL} \ , \ s = s_1, s_2, s_3 \ . \tag{1.18}$$

The above equations show that active and sterile neutrinos fields can be expanded using the same basis of mass eigenstates ν_{kL}. Hence, a sterile neutrino can oscillate to an active one, and viceversa.

The see-saw mechanism can be generalized to the case of three families following the procedure described for the case of one family. We will then consider the case in which $M_L = 0$ and the eigenvalues of M_D are negligible with respect to the ones belonging to M_R. The mixing matrix V can be rewritten in the factorized form

$$V = WU \ , \tag{1.19}$$

where W and U are unitary matrix, up to corrections of order $(M_R)^{-1}M_D$.

Expanding in powers of $(M_R)^{-1}M_D$ we find

$$W^T M W \approx \begin{pmatrix} M_{\rm light} & 0 \\ 0 & M_{\rm heavy} \end{pmatrix} \ , \tag{1.20}$$

where

$$M_{\rm light} \approx (M_D)^\dagger (M_R)^{-1} M_D, \qquad M_{\rm heavy} \approx M_R \ . \tag{1.21}$$

The above equations express the see-saw mechanism for the case of three family mixing. The larger the eigenvalues of M_R, the smaller the ones belonging to $M_{\rm light}$.

At low energies, $M_{\rm light}$ and $M_{\rm heavy}$ are decoupled, the off-diagonal elements of W being highly suppressed. Hence, we can restrict our discussion to the 3×3 matrix that diagonalizes $M_{\rm light}$, i.e. to the matrix U such that

$$U^\dagger M_{\rm light} U = \begin{pmatrix} m_1 & 0 & 0 \\ 0 & m_2 & 0 \\ 0 & 0 & m_3 \end{pmatrix} \ , \tag{1.22}$$

implying the three-family mixing equation:

$$\nu_{\alpha L} = \sum_{k=1}^{3} U_{\alpha k} \nu_{kL} \quad , \quad \nu_{kL} = \sum_{\alpha=1}^{3} U^*_{\alpha k} \nu_{\alpha L} \ . \tag{1.23}$$

The matrix U is called Pontecorvo-Maki-Nakagawa-Sakata (PMNS) matrix, or Lepton Mixing matrix. Being unitary, it only depends on nine independent parameters: three angles and six phases.

	lower limit (3σ)	best value	upper limit (3σ)
$(\Delta m^2_{sun})_{\rm LA}$ (10^{-5} eV^2)	5.4	6.9	9.5
Δm^2_{atm} (10^{-3} eV^2)	1.4	2.6	3.7
$\sin^2\theta_{12}$	0.23	0.30	0.39
$\sin^2\theta_{23}$	0.31	0.52	0.72
$\sin^2\theta_{13}$	0	0.006	0.054

Figure 1.1: Neutrino squared mass differences and mixing angles (from Ref. [4]).

It can be parametrized in terms of three mixing angles θ_{12}, θ_{23} and θ_{13} ($0 \leq \theta_{ij} \leq \pi/2$) and one phase φ ($0 \leq \varphi \leq 2\pi$), as in the case of the quark mixing matrix V_{CKM}. The resulting expression is

$$\begin{aligned} U &= \begin{pmatrix} U_{e1} & U_{e2} & U_{e3} \\ U_{\mu 1} & U_{\mu 2} & U_{\mu 3} \\ U_{\tau 1} & U_{\tau 2} & U_{\tau 3} \end{pmatrix} \\ &= \begin{pmatrix} 1 & 0 & 0 \\ 0 & c_{23} & s_{23} \\ 0 & -s_{23} & c_{23} \end{pmatrix} \begin{pmatrix} c_{13} & 0 & s_{13}e^{-i\delta_{CP}} \\ 0 & 1 & 0 \\ s_{13}e^{-i\delta_{CP}} & 0 & c_{13} \end{pmatrix} \begin{pmatrix} c_{12} & s_{12} & 0 \\ -s_{12} & c_{12} & 0 \\ 0 & 0 & 1 \end{pmatrix} , \end{aligned} \tag{1.24}$$

where $c_{ij} = \cos\theta_{ij}$ and $s_{ij} = \sin\theta_{ij}$, θ_{ij} being the mixing angle. In addition, if neutrino are Majorana particles, we have to include the relative phases among the Majorana masses m_1, m_2 and m_3. Choosing m_3 real and positive, these phases are carried by $m_{1,2} \equiv |m_{1,2}|e^{i\phi_{1,2}}$. In conclusion, the description of massive neutrino involves nine new parameters: three mass eigenvalues, three mixing angles and three CP violating phases.

1.2 Neutrino oscillations in vacuum

Let us consider the decay process

$$A \longrightarrow B + \ell_\alpha^+ + \nu_\alpha \ , \tag{1.25}$$

where ν_α and ℓ_α^+ are a neutrino of flavor α and the associated antilepton, respectively. After traveling a distance L in time T, the neutrino is described by the state

$$\mid \nu_\alpha(L,T)\rangle = \sum_{k=1}^{3} U_{\alpha k}^* \mathrm{e}^{-iE_kT+i\overrightarrow{p}_k\cdot\overrightarrow{L}} \mid \nu_k\rangle \ . \tag{1.26}$$

Replacing the mass eigenstate with a superposition of flavor eigenstates the above equation can be rewritten in the form

$$\mid \nu_\alpha(L,T)\rangle = \sum_{\beta=e,\mu,\tau} (\sum_{k=1}^{3} U_{\alpha k}^* \mathrm{e}^{-iE_kT+i\overrightarrow{p}_k\cdot\overrightarrow{L}}) U_{\beta k} \mid \nu_k\rangle \ , \tag{1.27}$$

showing that the transition amplitude of the process $\nu_\alpha \to \nu_\beta$, i.e. of neutrino oscillation, corresponds to the coefficient of $\mid \nu_\beta\rangle$. Hence, the corresponding probability reads

$$P_{\nu_\alpha\to\nu_\beta} = \mid \langle \nu_\beta \mid \nu_\alpha(L,T)\rangle \mid^2 = \mid \sum_{k=1}^{3} U_{\alpha k}^* \mathrm{e}^{-iE_kT+i\overrightarrow{p}_k\cdot\overrightarrow{L}} U_{\beta k} \mid^2 \ . \tag{1.28}$$

In the ultrarelativistic regime, in which $T = L$, we can rewrite

$$E_kT - p_kL \simeq (E_k - p_k)L = \frac{E_k^2 - p_k^2}{E_k + p_k} L \simeq \frac{m_k^2}{2E} L \ , \tag{1.29}$$

where E denotes the neutrino energy in the limit of vanishing mass. Under this assumption, the probability takes the simple form

$$P_{\nu_\alpha\to\nu_\beta} = \sum_k \mid U_{\alpha k} \mid^2 \mid U_{\beta k} \mid^2 + 2Re \sum_{k>j} U_{\alpha k}^* U_{\beta k} U_{\alpha j} U_{\beta j}^* \mathrm{e}^{-i\frac{\Delta m_{kj}^2 L}{2E}} \ , \tag{1.30}$$

with $\Delta m_{kj} = m_k^2 - m_j^2$. Hence, oscillations arise from the interference between the contributions associated with different neutrino mass eigenstates.

1.2.1 Two-neutrino mixing

To illustrate the main features of neutrino oscillations, let us first consider the simplest case of two neutrino mixing, which can be seen as a limiting situation in which two mixing angles are unimportant. It follows that:

- $\triangle m^2 \equiv \triangle m^2_{21}$;
- the parametrization of U depends on a single mixing angle, i.e.

$$U = \begin{pmatrix} \cos\theta & \sin\theta \\ -\sin\theta & cos\theta \end{pmatrix} \ . \tag{1.31}$$

The resulting transition probability turns out to be

$$P_{\nu_\alpha \to \nu_\beta} = \sin^2 2\theta \sin^2 \frac{\triangle m^2 L}{4E} \ . \tag{1.32}$$

Owing to the low neutrino interaction cross sections, to obtain a statistically significant measurement the experimental set up must be chosen is such a way as to make the transition probability not too small. This requirement amounts to imposing the constraint

$$\frac{\triangle m^2 L}{4E} \gtrsim 0.1 \div 1 \ , \tag{1.33}$$

implying in turn that the ratio L/E determines the range of Δm^2 values that can be detected.

Experiments can be classified according to the value of the ratio L/E

- Short-baseline experiments (SBL), with $L/E \lesssim 1$ eV^{-2}, are sensitive to $\Delta m^2 \gtrsim 0.1$ eV^2;
- Long-baseline experiments (LBL), with $L/E \lesssim 10^4$ eV^{-2}, are sensitive to $\Delta m^2 \gtrsim 10^{-4}$ eV^2;
- Very long-baseline experiments (VLBL), with $L/E \lesssim 3 \times 10^5$ eV^{-2}, are sensitive to $\Delta m^2 \gtrsim 3 \times 10^{-5}$ eV^2 .

1.2.2 Three-Neutrino Mixing

Up to now, neutrino oscillation experiments have determined two different values of Δm^2, corresponding to solar and atmospheric neutrinos

$$\Delta m^2_{\rm sun} \approx 7 \times 10^{-5}\ {\rm eV}^2 \quad , \quad \Delta m^2_{\rm atm} \approx 2.6 \times 10^{-3}\ {\rm eV}^2\ . \tag{1.34}$$

These quantities are related to the transition probabilities through

$$P(\nu_e \leftrightarrow \nu_\mu) = P(\nu_e \leftrightarrow \nu_\tau) = \frac{1}{2}\sin^2 2\theta_{12} \sin^2 \frac{\Delta m^2_{\rm sun} L}{4E} \tag{1.35}$$

$$P(\nu_\mu \leftrightarrow \nu_\tau) = \sin^2 \frac{\Delta m^2_{\rm atm} L}{4E} - \frac{1}{4}\sin^2 2\theta_{12} \sin^2 \frac{\Delta m^2_{\rm sun} L}{4E}\ . \tag{1.36}$$

As already mentioned, there are many alternative models of neutrino masses. This is mostly due to the considerable experimental ambiguities that still exist. One first missing input is the absolute scale of neutrino masses, as neutrino oscillations only determine mass squared differences. Another missing quantity is the value of the third mixing angle s_{13}, on which only the bound $s_{13} < 0.22$ is known[1].

Referring to Table 1.1, $\Delta m^2_I L/4E$ (I=sun, atm) are parametrized in terms of the neutrino mass eigenvalues according to

$$\Delta m^2_{sun} \equiv |\Delta m^2_{12}|, \qquad \Delta m^2_{atm} \equiv |\Delta m^2_{23}|\ , \tag{1.37}$$

where $\Delta m^2_{12} = |m_2|^2 - |m_1|^2 > 0$ and $\Delta m^2_{23} = m_2^2 - |m_2|^2$. Atmospheric neutrino oscillations mainly depend on Δm^2_{atm}, θ_{23} and θ_{13}, while solar oscillations are controlled by Δm^2_{sol}, θ_{12} and θ_{13}. Therefore, in the limit of vanishing s_{13}, the solar and atmospheric oscillations decouple, and depend on two separate sets of two-flavor parameters. For atmospheric neutrinos we have $c_{23} \sim s_{23} \sim 1/\sqrt{2}$, corresponding to nearly maximal mixing. Oscillations of muon neutrinos into tau neutrinos are favored over oscillations into sterile neutrinos.

[1] Recent measurements have shown that θ_{13} is in fact non vanishing and quite large, the reported value being such that $\sin^2 2\theta_{13} = 0.0929 \pm 0.016 \pm 0.005$, corresponding to $\theta_{13} \approx 9^\circ$ [5].

After the KamLAND [6] and SNO-salt [7] results, the only surviving solution to the solar neutrino problem is the Large Angle (LA) solution, with $\Delta m^2_{sol} \approx 7 \times 10^{-5}$ eV^2 and $\sin^2\theta_{12} \approx 0.3$. Data from solar neutrino experiments and KamLAND, involving, respectively, electron neutrinos and electron antineutrinos, are compatible with a CPT invariant spectrum. If we take maximal s_{13} and keep only linear terms in $u = s_{13}e^{i\varphi}$, from experiment we find the following structure of the $U_{fi}(f = e, \mu, \tau,\ i = 1, 2, 3)$ mixing matrix, up to sign convention redefinitions

$$U_{fi} = \begin{pmatrix} c_{12} & s_{12} & u \\ -(s_{12} + c_{12}u^*)/\sqrt{2} & (c_{12} - s_{12}u^*)/\sqrt{2} & 1/\sqrt{2} \\ (s_{12} - c_{12}u^*)/\sqrt{2} & -(c_{12} - s_{12}u^*)/\sqrt{2} & 1/\sqrt{2} \end{pmatrix} , \tag{1.38}$$

where θ_{12} is close to $\pi/6$. Given the observed frequencies there are three possible patterns of mass eigenvalues:

$$\text{Degenerate} : |m_1| \sim |m_2| \sim |m_3| \gg |m_i - m_j| , \tag{1.39}$$

$$\text{Inverted hierarchy} : |m_1| \sim |m_2| \gg |m_3| , \tag{1.40}$$

$$\text{Normal hierarchy} : |m_3| \gg |m_{2,1}| . \tag{1.41}$$

Models based on all these patterns have been proposed and studied and, at present, are in fact all viable.

1.3 Experimental searches of neutrino oscillations

1.3.1 Atmospheric Neutrinos

Atmospheric neutrinos are produced by interactions of cosmic-ray protons with air nuclei in the earth's atmosphere via the reaction chain:

$$p + N \longrightarrow \pi^{\pm} + X , \tag{1.42}$$

$$\pi^{\pm} \longrightarrow \mu^{\pm} + \nu(\bar{\nu}_{\mu}) , \tag{1.43}$$

$$\mu^{\pm} \longrightarrow e^{\pm} + \nu_e(\bar{\nu}_e) + \bar{\nu}_{\mu}(\nu_{\mu}) . \tag{1.44}$$

A simple counting leads to the ratio of flavors

$$R_{\mu/e} = \frac{N(\nu_\mu + (\bar{\nu}_\mu))}{N(\nu_e + (\bar{\nu}_e))} \sim 2 \ , \tag{1.45}$$

independent of the absolute fluxes, that are not well known. Generally, an oscillation would show up as a variation of the above ratio from the expected value of approximately 2.

Conventionally, experiments report the ratio between measured value of $R_{\mu/e}$ and the prediction of Monte Carlo simulations

$$R_{Data/MC} = \frac{[N(\nu_\mu + (\bar{\nu}_\mu))/N(\nu_e + (\bar{\nu}_e))]_{Data}}{[N(\nu_\mu + (\bar{\nu}_\mu))/N(\nu_e + (\bar{\nu}_e))]_{MC}} \ . \tag{1.46}$$

This ratio of ratios would be unity in the absence of neutrino oscillations, and if detector effects and backgrounds were correctly modeled. If flavor oscillations occur, $R_{\mu/e}$ becomes less than 2, and $R_{Data/MC}$ less than 1.

While being originally designed to search for proton decay, the Super-Kamiokande detector has been extensively and successfully employed to study atmospheric neutrinos. It is a large underground tank filled with 50,000 tons of water, used as a target for neutrino interactions.

The emission of Cherenkov light is exploited to determine a particle's velocity and direction. The measurements of atmospheric neutrino in water Cherenkov detectors is made possible by two key ingredients . First, even at a depth of 1000 meters (equivalent to 3000 meters of water), the cosmic muon flux is 10^8 μ/year, to be compared to the observed change in the flux which is around 150 events for year running. Second, the very large number of Cherenkov photons allows a discrimination between muons and electrons. Owing to their low mass, electrons undergo a larger number of multiple scattering events, leading to a fuzzier Cherenkov ring image. Analyzing the sharpness of this image allows one to identify electrons and muons with uncertainty less than 1%. Fully contained events

are classified according to their visible energy ("sub-GeV" for $E_{\rm vis} > 1.33$ GeV , "multi-GeV" for $E_{\rm vis} < 1.33$ GeV) and the number of reconstructed Cherenkov rings ("single-ring" for one reconstructed ring, "multi-ring" for two or more). Events in which the final state lepton (usually a muon) exits the fiducial region are considered partially-contained (PC) and treated separately from fully contained (FC) events.

The most recent results combining FC and PC muons are [8]

$$R_{Data/MC} = 0.67 \pm 0.02 \pm 0.05,\ {\rm sub-GeV}\ , \tag{1.47}$$

$$= 0.66 \pm 0.04 \pm 0.08,\ {\rm multi-GeV}\ . \tag{1.48}$$

At this point, it is useful to consider the numbers of events involved. Assuming the flux of electron neutrinos remains unchanged during transit through the earth, the number of observed e-like single ring events divided by the number expected gives a flux normalization of 1.17. Hence the observed flux is 17% larger than the predicted. Normalizing the number of expected single-ring μ-like events by this factor gives an observed deficit of 550 μ-like events. Normalizing the number of multi-ring events in the same way gives a deficit of about 100 events which is consistent with the number of ν_μ induced charged current events lost in $R_{Data/MC} = 0.6$.
Thus, the conclusion that neutrinos oscillate rests on the deficit of a few hundred events in the flux ratio measurement. A second and more sensitive method of detecting oscillations is related to the zenith angle distribution of neutrino events.

1.3.2 Solar Neutrinos

The sun produces electron neutrinos via nine principal reactions in the pp chain, starting with the fusion of two protons to make a deuteron and ending with the production of ^{4}He. The neutrino energies range from 0 to 15 MeV and three of the fusion reactions result in mono-energetic ν_e's at 380, 860 and 1400 keV (see Fig. 1.2).

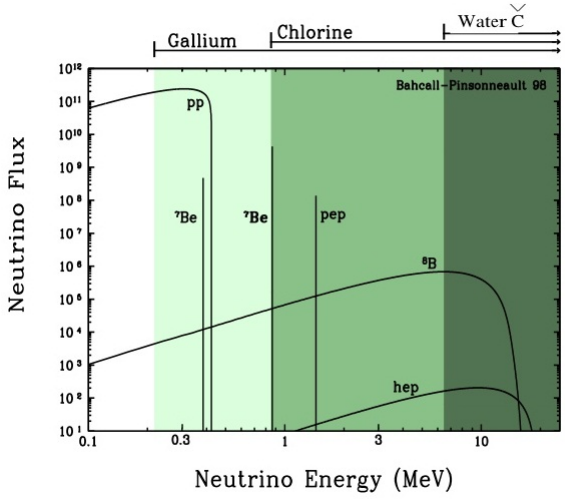

Figure 1.2: Energy spectrum at earth of solar neutrinos. The flux for lines is given as neutrino cm^{-2}/s. The continuous spectra are in units of neutrino cm^{-2}/MeV/s (from Ref. [8]).

Three different types of experiments have measured the solar neutrino flux. Owing to the different experimental techniques, each one was sensitive to a different portion of the neutrino energy spectrum. Water Cerenkov counters detect neutrinos via da $\nu_e + e^- \longrightarrow \nu_e + e^-$ and, due to their relatively high energy threshold of 5-7 MeV, detect only the upper part of the ^{8}B ν_e spectrum.

The original solar neutrino experiment exploited the reaction $\nu_e + {}^{37}\mathrm{Cl} \longrightarrow {}^{37}\mathrm{Ar} + e^-$ in perchloroethylene, which has a threshold of 814 keV, giving sensitivity to ^{7}Be, ^8B and *pep* neutrinos, as well as to the upper part of the CNO spectrum. Finally, the SAGE and Gallex experiments use the capture reaction $\nu_e + {}^{71}Ga \longrightarrow {}^{71}Ge + e^-$ in metallic gallium (SAGE) or gallium chloride (Gallex), with a threshold of 232 keV. This provides a window for detection of the pp ν_e.

The comparison between the fluxes observed by the various experiments and their predicted values shows a deficit of the solar ν_e. The "classic" experiments, Homestake, Gallex, (Super)Kamiokande etc, pointed to a deficit with respect to the predictions based

on the standard solar model. More recent experiments, such as SNO and KamLAND, proved instead that the effect has to do with neutrino physics, and not with sun physics.

The data collected by SNO include charged current (CC), neutral current (NC) and electron scattering (ES) events:

$$\nu_e + d \longrightarrow p + n + e^- \quad (CC) \ , \tag{1.49}$$

$$\nu_x + d \longrightarrow p + n + \nu_x \quad (NC) \ , \tag{1.50}$$

$$\nu_x + e^- \longrightarrow \nu_x + e^- \quad (ES) \ , \tag{1.51}$$

where ν_x refers to ν_e, ν_μ or ν_τ. The first reaction measures the flux of solar ν_e, while the second and the third reactions measure the total flux of ν_e, ν_μ and ν_τ. Actually, SNO proved that the total ν flux from the sun is in agreement with expectations but only $\sim 1/3$ is ν_e and $\sim 2/3$ is from active (i.e. not sterile) ν's (i.e. ν_μ and ν_τ). This is a direct evidence of $\nu_e \longrightarrow \nu_{\mu,\tau}$ oscillations as solution of the solar ν_e deficit.

Moreover, the KamLAND experiment has established that $\bar{\nu_e}$ from a reactor show oscillations over an average distance of about 180 Km which are perfectly compatible with the frequency and mixing angle corresponding to one of the solutions of the solar neutrino problem (the LA solution).

Chapter 2

The MiniBooNE experiment and the axial mass puzzle

The MiniBooNe experiment at Fermilab was originally designed to confirm the evidence of neutrino oscillations reported by the LSND Collaboration. The LSND experiment, carried out at Los Alamos, had a baseline $\sim$ 30 m and a neutrino energy $\sim 30 - 60$ MeV, corresponding to $L/E \sim 1$ eV^{-2}. Hence, under the two massive neutrino oscillation hypothesis, LSND signals correspond to neutrino oscillations with $\Delta m^2 \sim 1$ eV^2. Confirming the LSND signal would amount to suggest the existence of a new, sterile, neutrino around the 1 eV mass scale, and should therefore be regarded as an important discovery of new physics beyond the Standard Model.

In this Chapter, after briefly describing the MiniBooNE experimental set up, we will focus on the measurements of the neutrino cross section, with particular emphasis on charged current quasi elastic (CCQE) processes. The results of the analysis of the MiniBooNE CCQE event sample, showing an excess with respect to the predictions of Monte Carlo simulations, raised the still controversial issue of the possible medium modification of the nucleon axial mass, the study of which is the main motivation of our work.

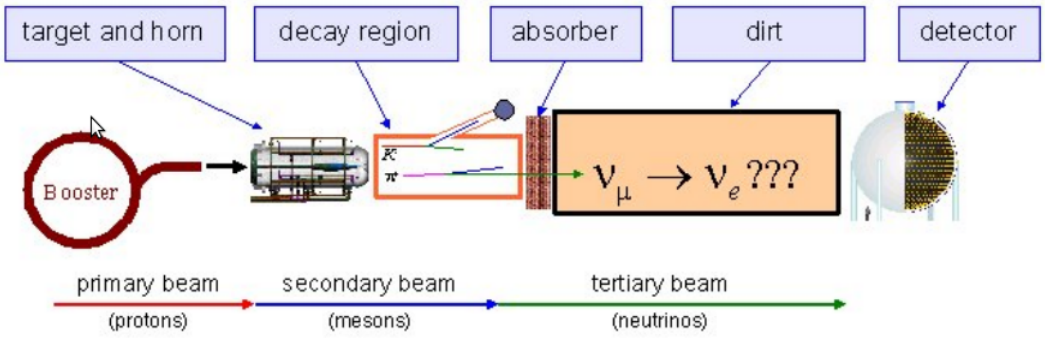

Figure 2.1: Schematic overview of the MiniBooNE experiment, including the Booster Neutrino Beamline and MiniBooNE detector.

2.1 Overview of the MiniBooNE experiment

The MiniBooNE experiment was designed to search for $\bar{\nu}_\mu \rightarrow \bar{\nu}_e$ and $\nu_\mu \rightarrow \nu_e$ oscillations, with approximately the same value of $L/E \simeq 1$ eV^{-2} as LSND (recall: L is the distance, in units of m, travelled by neutrinos from the source to the detector, while E is the neutrino energy in MeV). The LSND neutrino beam travelled a distance of 30 m with a typical energy of 30 MeV, while the MiniBooNE neutrino beam travelled a distance of 500 m with a typical energy of 500 MeV. With neutrino energies one order of magnitude higher, the MiniBooNE backgrounds and systematic errors are completely different from those of LSND. Therefore, MiniBooNE can provide an independent check of the LSND signal of neutrino oscillations at the ~ 1eV^2 mass scale.

Let us briefly describe the experiment layout. Protons with 8 GeV kinetic energy are extracted from the Fermilab Booster and transported to the MiniBooNE target hall, which contains a beryllium target within a magnetic focusing horn. The target and horn are followed by a pion-kaon decay volume, at the end of which is a 3.8 m thick steel and concrete beam dump. The distance from the center of the target to the front face of the

dump is 50 m. Thus, the neutrino beam, produced in the decay volume via:

$$K^+ \longrightarrow \mu^+ + \nu_\mu \qquad , \qquad \pi^+ \longrightarrow \mu^+ + \nu_\mu \tag{2.1}$$

$$K^- \longrightarrow \mu^- + \bar{\nu}_\mu \qquad , \qquad \pi^- \longrightarrow \mu^- + \bar{\nu}_\mu \tag{2.2}$$

passes though the dump plus 474 m of earth before reaching the MiniBooNE detector vault. This ensures that neutrinos are the only beam products that can reach the liquid Cherenkov detectors, filled with mineral oil (CH_2). As the photomultiplier tube (PMT) coverage for a liquid Cherenkov detector is proportional to the detector surface area, a spherical tank was chosen to maximize the ratio of volume to surface area. Furthermore, a spherical geometry has no inside edges, which is beneficial for the event reconstruction. The detector, see Fig. 2.1, is a spherical tank of diameter 12.2 m, which is filled with 818 tons of mineral oil. An opaque barrier divides the volume into an inside main detector region and an outside veto region and supports the PMT's viewing the main detector region. The detector tank sits below ground level inside a 13.7 m diameter cylindrical vault, with a room above that houses electronics and utilities. The vault not only provides access to the tank's exterior plumbing, but also acts as secondary containment for the mineral oil. The entire structure is covered by at least 3 m of dirt, which provides shielding against cosmic ray backgrounds and makes it easier to keep the detector at a constant temperature.

Figure 2.2 shows the predicted MiniBooNE neutrino flux as a function of neutrino energy, the mean value of which is $\langle E_\nu \rangle = 788$ MeV. The beam also reveals the presence of 6% of $\bar{\nu}_\mu$ and approximately 0.5 % of ν_e and $\bar{\nu}_e$.

In the kinematical range corresponding to the flux of Fig. 2.2 the dominant reaction mechanisms are quasi elastic scattering

$$\nu_\mu + n \rightarrow p + \mu^- \qquad , \qquad \bar{\nu}_\mu + p \rightarrow n + \mu^+ \ , \tag{2.3}$$

and excitation of nucleon resonances, leading to pion emission.

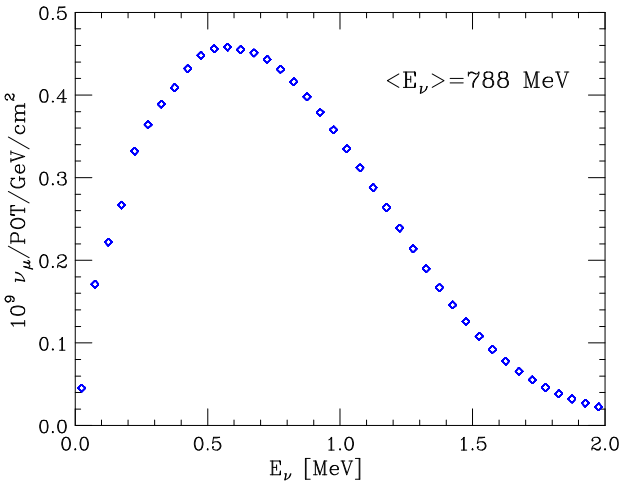

Figure 2.2: Predicted ν_μ flux at the MiniBooNE detector. The integrated flux is $5.16 \times 10^{-10}\nu_\mu/\mathrm{POT/cm}^2$ ($0 < \mathrm{E}_\nu < 3\mathrm{GeV}$) with a mean energy of 788 MeV.

2.2 The axial mass puzzle

Figure 2.3 illustrates the topology of a charged-current quasi elastic (CCQE) event according to the MiniBooNE classification, based on the assumption that the incoming neutrino interacts with a single neutron in the carbon target. Besides the recoiling nucleus, the final state consists of a proton and a muon, and CCQE interactions are identified detecting the Cherenkov light from the charged leptons.

Within the single nucleon knockout picture, the neutrino energy, reconstructed from the observed muon energy, exhibits a distribution reflecting the energy and momentum distribution of the struck neutron in the initial state. As a consequence, its determination depends on the nuclear model employed to describe the target.

From the requirement that the elementary scattering process $\nu_\mu + n \rightarrow \mu + X$ be elastic, i.e. that

$$(k_\nu + p_n - k_\mu)^2 = M_p^2 \tag{2.4}$$

where M_p is the proton mass and the four-momenta of the participating particles are

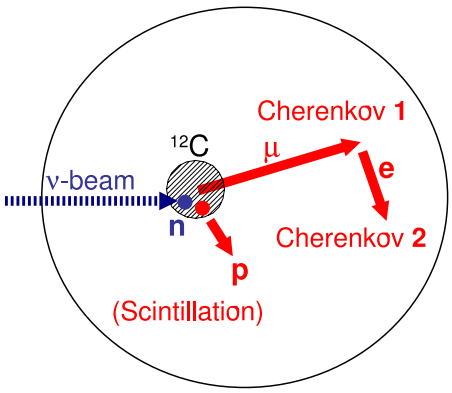

Figure 2.3: Schematic illustration of a CCQE interaction in the MiniBooNE detector. The primary Cherenkov light from the muon (Cherenkov 1, first subevent) and the subsequent Cherenkov light from the decay-electron (Cherenkov 2, second subevent) are used to tag the CCQE event. No requirements are made on the outgoing proton

denoted by $k_\nu = (E_\nu, \mathbf{k}_\nu)$, $k_\mu = (E_\mu, \mathbf{k}_\mu)$ and $p_n = (E_n, \mathbf{p}_n)$, it follows that

$$E_\nu = \frac{M_p^2 - m_\mu^2 - E_n^2 + 2E_\mu E_n - 2\mathbf{k}_\mu \cdot \mathbf{p}_n + |\mathbf{p}_n^2|}{2(E_n - E_\mu + |\mathbf{k}_\mu| \cos\theta_\mu - |\mathbf{p}_n| \cos\theta_n)} \ , \tag{2.5}$$

where θ_μ is the muon angle relative to the neutrino beam and and $\cos\theta_n = (\mathbf{k}_\nu \cdot \mathbf{p}_n)/(|\mathbf{k}_\nu||\mathbf{p}_n|)$.

Data analysis requires the knowledge of the energy-momentum distribution of neutrons in the ^{12}C ground state, as well as of the vector and axial form factors, entering the description of the quasi elastic neutrino-nucleon interaction vertex, to be discussed in Chapter 3. The MiniBooNE Monte Carlo simulations employ the energy-momentum distribution provided by the Relativistic Fermi Gas Model (RFGM), the main features of which will be outlined in Chapter 4.

The vector proton and neutron form factors are related to the corresponding electromagnetic form factors through the conserved vector current (CVC) hypothesis. As a consequence, they can be extracted from the measured electron-proton and electron-deuteron cross sections in the quasi elastic sector. The MiniBooNE analysis is carried out using a state-of-the-art parametrization of the available data [13].

It has to be pointed out that the possibility of using the form factors obtained from

proton and deuteron data to compute the carbon cross section rests on the assumption that the form factors are *not* modified in the nuclear medium. Comparison between the results of theoretical calculations and the large data base of electron-nucleus scattering cross sections provides overwhelming evidence of the validity of this hypothesis.

The axial form factor is generally parametrized in the dipole form (see Appendix A)

$$F_A(Q^2) = \frac{g_A}{\left[1 + (Q^2/M_A^2)\right]^2} \ , \tag{2.6}$$

with the axial coupling constant g_A obtained from the measurements of neutron β-decay.

Within the scheme employed to obtain the vector form factors, the so called *axial mass*, determining the Q^2-dependence of $F_A(Q^2)$, is extracted from neutrino-deuteron scattering data. The world average of the resulting values of the axial mass turns out to be $M_A = 1.03 \pm 0.02$ GeV. On the other hand, the analyses of CCQE data samples recently performed by both the MiniBooNE [9] and K2K [14] collaborations, the latter using an oxygen target, yield the much larger values $M_A \sim 1.35$ and 1.2 GeV, respectively. It would be tempting to interpret these large values of M_A as an *effective* axial mass, modified by nuclear effects not included in the RFGM employed in data analysis. However, theoretical calculations of the quasi elastic single nucleon knockout cross section fail to support this explanation, suggested by the authors of Ref. [9].

As an example, Fig. 2.4, shows a comparison between the Q^2-distribution of CCQE events at beam energy $E_\nu = 700$ MeV, computed using the RFGM and $M_A = 1.23$ GeV (dashed lines) and a more refined dynamical model providing a quantitative description of electron scattering data, to be discussed in Chapter 4, and $M_A = 1.03$ GeV (solid lines). It appears that, as far as the Q^2 distribution of single nucleon knockout processes at fixed neutrino energy is concerned, a larger value of the axial mass cannot be explained by replacing the RFGM with a more advanced model of nuclear dynamics.

To make the interpretation of the large values of M_A obtained by MiniBooNE and K2K even more puzzling, the NOMAD collaboration has recently reported the results of

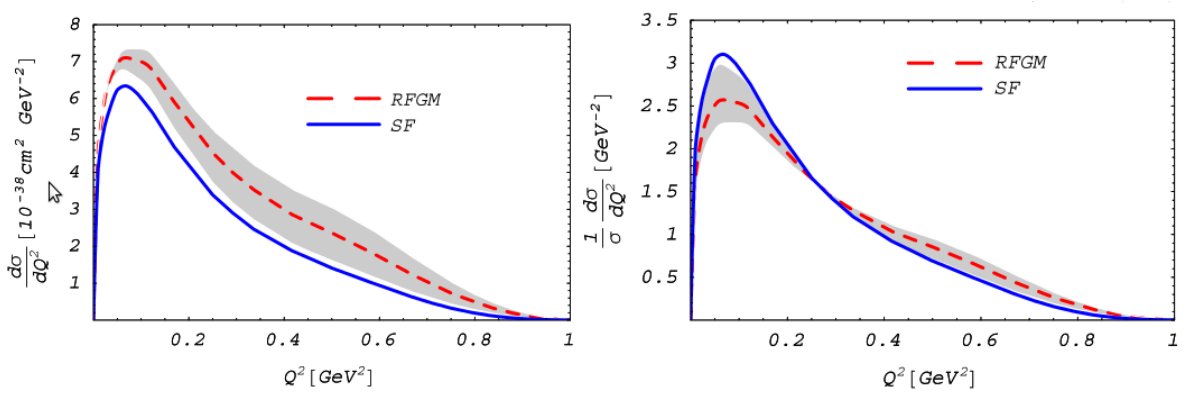

Figure 2.4: Q^2-dependence of the cross section of the process $\nu_\mu + ^{12}C \to \mu + p + X$, for neutrino energy $E_\nu = 0.7$ GeV. The dashed line corresponds to the results of the RFGM with $M_A = 1.23$ GeV, whereas the solid line has been obtained using the more advanced dynamical model discussed in Chapter 4 and setting $M_A = 1.03$ GeV. The shaded area corresponds to the 1σ uncertainty on the axial mass quoted in [9]. The left and right panels corresponds to non-normalized and normalized distributions respectively (taken from Ref. [16]).

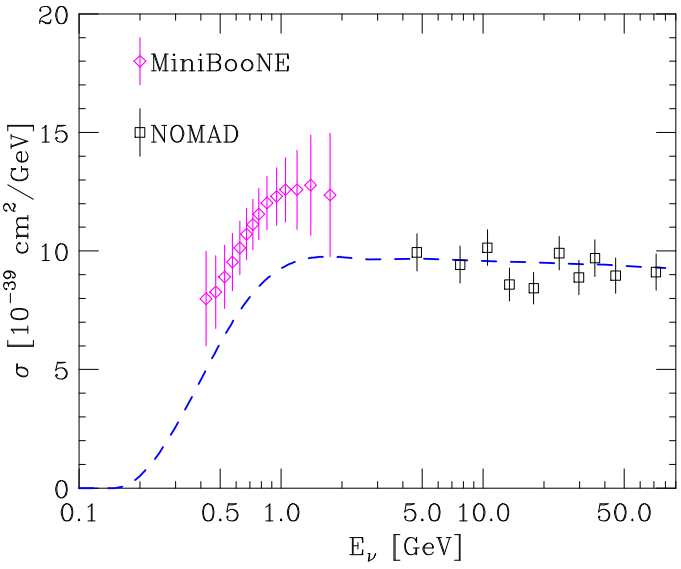

Figure 2.5: CCQE total cross section reported by the MiniBooNE [9] and NOMAD [15] collaborations, shown as a function of neutrino energy. The dashed line shows the results of a theoretical calculation carried out using a dipole parametrization of the nucleon axial form factor and setting $M_A = 1.03$ GeV.

the analysis of its CCQE event sample, detected using a carbon target, yielding a value of the axial mass compatible with that extracted from deuteron data [15].

As an illustration of the present status of the axial mass puzzle, in Fig. 2.5 the total CCQE cross-section reported by the MiniBooNE and NOMAD collaborations are shown as a function of the incoming neutrino energy. The disagreement between the two measurements clearly appears to be striking For reference, Fig. 2.5 also shows the results of a theoretical calculation of the total CCQE cross section, carried out using the formalism to described in Chapters 3 and 4, with a dipole parametrization of the nucleon axial form factor and setting $M_A = 1.03$ GeV. Comparison between theory and data shows that the value of the axial mass extracted from deuterium measurements, while providing a good account of the NOMAD data, fails to describe the MiniBooNE cross section.

Chapter 3

Theoretical Description of neutrino-nucleus interactions

The aim of this Chapter is analyzing the quasi-elastic neutrino-nucleus cross section within the Born approximation. We will focus on the kinematical regime in which the Impulse Approximation (IA) is applicable, and the nuclear cross section can be written in terms of the target spectral function and the elementary neutrino-nucleon cross section.

In Sections 3.1 and 3.2, after recalling the elements of the Glashow-Weinberg-Salam theory of weak interactions relevant to our discussion, we will derive the expression of the charged-current neutrino-nucleon cross section, while Section 3.3 will be devoted to the discussion of the nuclear cross section within the IA.

We will consider inclusive processes, in which only the outgoing charged lepton is detected, in the kinematical region corresponding to beam energies $E_\nu \sim 1$ GeV, in which the formalism based on the IA is expected to be applicable.

3.1 Interaction Hamiltonian

Weak interactions are described by the theory of Glashow, Weinberg and Salam (GWS). Here, we use GWS theory to derive an effective Hamiltonian in the current-current interaction form.

The starting point is the interaction Hamiltonian density

$$\mathscr{H}_{\rm w} = g(W^{\mu} {J_{\mu}}^{\dagger} + W^{\mu\dagger} J_{\mu}) \ , \tag{3.1}$$

where W_{μ} and ${W_{\mu}}^{\dagger}$ are the fields associated with the charged vector bosons, and J_{μ} is the charged weak current, defined by

$$J_{\mu} = \frac{1}{\sqrt{2}} \Big(\bar{\nu}_{\ell} \gamma_{\mu} \frac{1-\gamma_5}{2} \ell + \bar{u} \gamma_{\mu} \frac{1-\gamma_5}{2} d \Big) \ . \tag{3.2}$$

Here, ν_{ℓ} denotes the neutrino field, ℓ the associated charged lepton field, of flavor $\ell = e,\ \mu,$ or τ, u is an up-type quark of flavor $u,\ c,$ or t and d a down-type quark of flavor $d,\ s,$ or b.

When the momentum transfer is much smaller than the W boson mass, $M_{\rm w} \approx 80$ GeV, the two-point Green's function of the weak boson can be approximated as

$$\langle W_{\mu}(x) {W_{\nu}}^{\dagger}(y) \rangle = \frac{i g_{\mu\nu}}{M_{\rm w}^2} \delta^4(x-y), \tag{3.3}$$

and the effective Hamiltonian can be written in the form

$$\mathscr{H}_{\rm w}^{\rm eff} = \frac{G}{\sqrt{2}} j^{\mu} {j_{\mu}}^{\dagger} \tag{3.4}$$

with

$$j_{\mu} = j_{\mu}^{\rm lep} + j_{\mu}^{\rm had} \ , \tag{3.5}$$

and $G/\sqrt{2} = g^2/8M_{\rm w}^2$. The leptonic and hadronic currents are given by

$$j_{\mu}^{\rm lep} = \bar{\nu}_{\ell} \gamma_{\mu} (1-\gamma_5) \ell \quad , \quad j_{\mu}^{\rm had} = \bar{u} \gamma_{\mu} (1-\gamma_5) d \ . \tag{3.6}$$

The above currents can be used to carry out quantitative calculations of charged current processes involving leptons and quarks. However, experiments are *not* performed with quarks, the dynamics of which is dictated by the fundamental theory of strong interactions, Quantum-Chromo-Dynamics, or QCD, but with *hadrons*.

The hadronic currents of the type, $\langle p|j_\mu^{\rm had}|n\rangle$, where n and p denote neutron and proton, respectively, can not be expressed in terms of the quark currents. However, the V − A structure is preserved, so that we can write

$$\langle p|j_\mu^{\rm had}|n\rangle = j_\mu^V - j_\mu^A \ . \tag{3.7}$$

We will consider the vector contribution, the structure of which can be cast in the form

$$j_\mu^V = \bar{u}(p')\Big[\ \dots\ \Big]u(p) \tag{3.8}$$

where $\bar{u}$ and u are Dirac spinors describing the initial and final state nucleons, carrying four-momenta p and p', respectively.

Since the proton is a composite particle of finite size, the quantity enclosed in square brakets is not simply a γ matrix. However, we know that j_μ^V transform as a four vector under Lorentz transformations. Hence, we can write it as the most general four-vector that can be constructed from p, p' and q, where $q = p - p'$ is the four-momentum transfer, and the Dirac γ-matrices sandwiched between Dirac's spinors. It turns out that there are only two independent terms, γ^μ and $i\sigma^{\mu\nu}q_\nu$, with $\sigma^{\mu\nu} = i[\gamma^\mu, \gamma^\nu]/2$. Moreover, their coefficients must be functions of the only non trivial invariant q^2. Therefore, quite generally, we can write the square bracket of Eq.(3.8) in the form

$$\Big[\ \dots\ \Big] = \left[F_V(q^2)\gamma^\mu + \frac{\kappa}{2M}F_M(q^2)i\sigma^{\mu\nu}q_\nu\right] , \tag{3.9}$$

where κ is the anomalous magnetic moment, while F_V and F_M are two independent *form factors*, parametrizing our ignorance of the internal structure of the proton.

The axial contribution to the current can also be discussed using the above procedure. The detailed expression of the hadronic current employed in numerical calculation, as well as a further comment on its structure, can be found in Appendix A.

3.2 Charged-current neutrino-nucleon cross section

In this Section, we will derive the cross section of the the charged-current reaction

$$\nu_\ell(k) + n(p) \longrightarrow \ell^-(k') + p(p') \ , \tag{3.10}$$

where the four-momenta of the participating particles are defined as

$$\begin{aligned} k &= (E_\nu, \mathbf{k}), \qquad k' = (E_\ell, \mathbf{k}') \\ p &= (E_p, \mathbf{p}), \qquad p' = (E_{p'}, \mathbf{p}') \end{aligned} \tag{3.11}$$

and $q = (\omega, \mathbf{q}) = k - k'$ is the four-momentum transfer.

Using the currents defined in Appendix A, we can write the lowest order invariant amplitude of the process in the form

$$\begin{aligned} \mathscr{M} = &\frac{G_F V_{ud}}{\sqrt{2}(1+\frac{Q^2}{M_W^2})} \bar{u}_\ell(k')\gamma_\mu(1-\gamma_5)u_{\nu_\ell}(k)\times \\ &\bar{u}_p(p')\Big[F_V(q^2)\gamma^\mu + iF_M(q^2)\sigma^{\mu\nu}\frac{q_\nu}{2M} + F_A(q^2)\gamma^\mu\gamma_5 + F_P(q^2)\frac{2M}{m_\pi^2}q^\mu\gamma_5\Big]u_n(p) \ , \end{aligned} \tag{3.12}$$

where M are m_π are the nucleon and pion mass, respectively, M_w is the mass of the charged vector boson, u and $\bar{u}$ are Dirac spinors describing the initial and final state nucleon and G_F and V_{ud} denote the Fermi constant and the CKM matrix element coupling u and d quarks.

We want to calculate the unpolarized cross section, carrying no information about the particle spins of the particles. It can be obtained by replacing

$$|\mathscr{M}|^2 \to |\overline{\mathscr{M}}|^2 = \overline{\sum_i} \sum_f |\mathscr{M}|^2 = \frac{G_F^2 V_{ud}^2}{2(1+\frac{Q^2}{M_W^2})^2}\frac{1}{mm_\nu}L^{\mu\nu}W_{\mu\nu} \ , \tag{3.13}$$

which amounts to averaging over the spins of the incoming particles and summing over the spins of the particles in the final state. In the above equation, m and m_ν denote the charged lepton mass and the neutrino mass, respectively, while $L_{\mu\nu}$ and $W^{\mu\nu}$ are the leptonic and hadronic tensors.

Neglecting all contributions containing the lepton masses, the leptonic tensor, can be written in the form

$$\begin{aligned} L^{\mu\nu} =& \frac{1}{8} Tr\Big[\not{k}'\gamma^{\mu}(1-\gamma_5)\not{k}\gamma^{\nu}(1-\gamma_5)\Big] \\ =& k'^{\mu}k^{\nu} + k'^{\nu}k^{\mu} - g^{\mu\nu}k\cdot k' + i\epsilon^{\mu\nu\varrho\sigma}k_{\varrho}k'_{\sigma} \ , \end{aligned} \tag{3.14}$$

showing that $L^{\mu\nu}$ is completely determined by lepton kinematics. On the other hand, the hadronic tensor depends on the internal structure of the hadrons through the form factors.

The terms proportional to $\sigma^{\mu\nu}$, appearing in the hadronic current, can be rewritten exploiting Gordon's identity

$$2M\bar{u}(p')\gamma^{\mu}u(p) = \bar{u}(p')((p'+p)^{\mu} + i\sigma^{\mu\nu}q_{\nu})u(p) \ . \tag{3.15}$$

Moreover, the terms associated with the pseudo-scalar form factor $F_P(q^2)$ contributes at most $\sim 1\%$ to the ν_μ cross section, and can therefore be neglected[1].

Thus, we get:

$$W^{\mu\nu} = Tr\Big\{\frac{\not{p}'+\not{p}}{2M}[\gamma^{\mu}(1-r\gamma_5) - \frac{R}{2M}\tilde{p}^{\mu}]\frac{\not{p}+M}{2M}[\gamma^{\nu}(1-r\gamma_5) - \frac{R}{2M}\tilde{p}^{\nu}]\Big\}(F_V+F_M)^2, \tag{3.16}$$

where:

$$\tilde{p}^{\mu} = p^{\mu} + p'^{\mu} \quad , \quad r = -\frac{F_A}{F_V+F_M} \quad , \quad R = \frac{F_M}{F_V+F_M} \ . \tag{3.17}$$

Carrying out the trace in Eq. (3.16) and imposing four momentum conservation we finally obtain the hadronic tensor in the form

$$\begin{aligned} W^{\mu\nu} = \Bigg\{ & -2g^{\mu\nu}\Big[r^2\big(1-\frac{q^2}{4M}\big) - \frac{q^2}{4M}\Big] + 2\frac{p^{\mu}p^{\nu}}{M^2}\Big[1+r^2+R^2\big(1-\frac{q^2}{4M^2}\big) - 2R\Big] \\ & - i\epsilon^{\mu\nu\varrho\sigma}\frac{p_{\varrho}p_{\sigma}}{2M^2}(4r) + \frac{q^{\mu}q^{\nu}}{M^2}\Big[\frac{R^2}{2}\big(1-\frac{q^2}{4M^2}\big) - R\Big] \\ & + \frac{p^{\mu}q^{\nu}+p^{\nu}q^{\mu}}{M^2}\Big[1+r^2+R^2\big(1-\frac{q^2}{4M^2}-2R\big)\Big]\Bigg\}(F_V+F_M)^2 \ , \end{aligned} \tag{3.18}$$

[1]Note , however, that it must be taken into account in the case of the ν_τ interactions.

showing that $W^{\mu\nu}$ can be written in terms of five structure functions, depending on q^2 only

$$\begin{aligned} W^{\mu\nu} &= \sum_{i=1}^{5} \Gamma_i^{\mu\nu} W_i(q^2) = -g^{\mu\nu} W_1(q^2) + \frac{p^\mu p^\nu}{M^2} W_2(q^2) \\ &- i\epsilon^{\mu\nu\varrho\sigma} \frac{p_\varrho q_\sigma}{2M^2} W_3(q^2) + \frac{q^\mu q^\nu}{m^2} W_4(q^2) + \frac{p^\mu q^\nu + p^\nu q^\mu}{M^2} W_5(q^2) \ . \end{aligned} \tag{3.19}$$

Comparing Eqs.(3.18) and (3.19) we obtain the explicit expressions of the structure functions in terms of the form factors

$$W_1 = 2[F_A^2(1+\tau) + \tau(F_V + F_M)^2] \tag{3.20}$$

$$W_2 = 2[F_A^2 + F_V^2 + \tau F_M^2] \tag{3.21}$$

$$W_3 = 4F_A(F_V + F_M) \tag{3.22}$$

$$W_4 = \frac{1}{2}[F_M^2(1+\tau) - 2F_M(F_V + F_M)] \tag{3.23}$$

$$W_5 = \frac{W_2}{2} \ . \tag{3.24}$$

The next step consists of contracting the leptonic and hadronic tensors, with the result

$$\begin{aligned} L^{\mu\nu} W_{\mu\nu} &= W_1(2k\cdot k') + W_2\Big(2\frac{(p\cdot k')(p\cdot k)}{M^2} - k\cdot k'\Big) \\ &- W_3\Big(\frac{2}{M^2}\Big)((k'\cdot q)(k\cdot p) - (k'\cdot p)(k\cdot q)\Big) + W_4\Big(2\frac{(k'\cdot q)(k\cdot p)}{M^2} - \frac{(k'\cdot k)q^2}{M^2}\Big) \\ &+ W_5\cdot 2\Big(\frac{(p\cdot k')(k\cdot q)}{M^2} - \frac{(k'\cdot k)(p\cdot q)}{M^2} + \frac{(k\cdot p)(k'\cdot q)}{M^2}\Big) \ . \end{aligned} \tag{3.25}$$

We now choose to carry out the calculation in the lab frame, in which the neutron is at rest, and keep on neglecting the lepton masses, implying $E_n = M$, $E = |\mathbf{k}|$ and $E' = |\mathbf{k}'|$. Substituting

$$p^\mu = (E_n, 0) \quad , \quad p'^\mu = (E_p, \mathbf{p}') \quad , \quad k^\mu = (E, \mathbf{k}) \quad , \quad k'^\mu = (E', \mathbf{k}') \tag{3.26}$$

in Eq.(3.25) yields

$$\begin{aligned} L^{\mu\nu} W_{\mu\nu} &= 2EE'\Big\{W_1(1-\cos\theta) + W_2\frac{1+\cos\theta}{2} + W_3\Big[\frac{m^2}{2ME'} - \frac{E+E'}{M}\frac{1+\cos\theta}{2}\Big] \\ &+ W_4\frac{m^2}{M^2}\frac{1-\cos\theta}{2} - W_5\frac{m^2}{ME'}\Big\} \ . \end{aligned} \tag{3.27}$$

We are now in the position of performing the calculation of the differential cross section, related to the invariant amplitude through:

$$d\sigma = (2\pi)^4\delta^{(4)}(p+k-k'-p')|\overline{\mathscr{M}}|^2\frac{m}{E'}\frac{m_\nu}{E}\frac{M}{E_n}\frac{M}{E_p}\frac{d^3p'}{(2\pi)^3}\frac{d^3k'}{(2\pi)^3}\ . \tag{3.28}$$

The integration over the momentum of the outgoing nucleon is performed using the tridimensional δ-function. Neglecting the mass of the charged lepton we finally obtain

$$d\sigma = \frac{1}{(2\pi)^2}\delta\Big(M+E-E'-\sqrt{M^2+|\mathbf{k}-\mathbf{k}'|^2}\Big)|\overline{\mathscr{M}}|^2 M\frac{mm_\nu}{EE_p}k'dE'd\Omega. \tag{3.29}$$

Note that, the above cross section is in the double differential form reported by the MiniBooNE collaboration.

The remaining δ-function univocally relates the energy of the charged lepton to the scattering angle, since:

$$\begin{aligned}&\delta\Big(M+E-E'-\sqrt{M^2+|\mathbf{k}-\mathbf{k}'|^2}\Big)\\ &\qquad = \delta\Big(M+E-E'-\sqrt{M^2+E^2+E'^2-2EE'\cos\theta}\Big)\ ,\end{aligned} \tag{3.30}$$

and requiring the argument to vanish yields

$$M+E-E' = \sqrt{M^2+E^2+E'^2-2EE'\cos\theta} \Longrightarrow E'(\theta) = \frac{E}{1+\frac{2E}{M}\sin^2\frac{\theta}{2}}. \tag{3.31}$$

Using the δ-function property

$$\delta\Big(f(x)\Big) = \sum_{x_0}\Big(\Big|\frac{\partial f}{\partial x}\Big|_{x_0}\Big)^{-1}\delta(x-x_0) \qquad , \qquad f(x_0)=0, \tag{3.32}$$

implying that

$$\delta\Big(M+E-E'-\sqrt{M^2+|\mathbf{k}-\mathbf{k}'|^2}\Big) = \delta\Big(E'-\frac{E}{1+\frac{2E}{M}sin^2\frac{\theta}{2}}\Big)\frac{E'(\theta)E_p}{EM}\ , \tag{3.33}$$

we finally arrive at the expression of the differential cross section

$$\begin{aligned}\frac{d\sigma}{d\Omega} = \frac{G_F^2V_{ud}^2}{(2\pi)^2\Big[1+\frac{Q^2}{M_W}\Big]}\frac{E'^3}{E}\Big[&2W_1\sin^2\frac{\theta}{2}+W_2\cos^2\frac{\theta}{2}\\ &-W_3\frac{E+E'}{M}\sin^2\frac{\theta}{2}+W_4\frac{m^2}{M^2}\sin^2\frac{\theta}{2}-W_5\frac{m^2}{ME'}\Big]\ .\end{aligned} \tag{3.34}$$

The cross section for the processes involving antineutrinos

$$\bar{\nu}_\ell + p \longrightarrow \ell^+ + n \ , \tag{3.35}$$

can be readily obtained starting from Eq. (3.30). We observe that: (i) substituting $\nu \to \bar{\nu}$ corresponds to interchanging $k \leftrightarrow k'$ in the leptonic tensor, which in turn changes sign in front of $\epsilon^{\mu\nu\varrho\sigma}$. As $\epsilon^{\mu\nu\varrho\sigma}$ is antisymmetric in the indices μ, ν, its only non vanishing contribution to the contraction $L_{\mu\nu}W^{\mu\nu}$ is $\propto W_3$. Thus, in order to study antineutrino scattering one has to change the sign of W_3.

3.3 Neutrino-nucleus interaction in the Impulse Approximation regime

The differential cross section of the process (schematically represented in Fig. 3.1)

$$\nu_\ell + A \longrightarrow \ell^- + X \tag{3.36}$$

in which a neutrino carrying initial four-momentum $k = (E_\nu, k)$ scatters off a nuclear target producing a charged lepton of four-momentum $k' = (E_\ell, k')$, while the target final in undetected, can be written, in Born approximation, as (compare to Eq. (3.13))

$$\frac{d^2\sigma}{d\Omega dE_\ell} = \frac{G_F^2 V_{ud}^2}{16\pi^2}\frac{|k'|}{|k|}L_{\mu\nu}W_A^{\mu\nu} \ . \tag{3.37}$$

The leptonic tensor, the form of which is given in Eq.(3.14) is completely determined by lepton kinematics, whereas the nuclear tensor $W_A^{\mu\nu}$, containing all the information on strong interaction dynamics, describes the response of the target nucleus. Its definition involves the initial and final hadronic states $|0\rangle$ and $|X\rangle$, carrying four momenta p_0 and p_X, respectively, as well as the nuclear electroweak current operator J_A^μ:

$$W_A^{\mu\nu} = \sum_X \langle 0|J_A^{\mu\dagger}|X\rangle\langle X|J_A^\nu|0\rangle\delta^{(4)}(p_0 + q - p_X) \ , \tag{3.38}$$

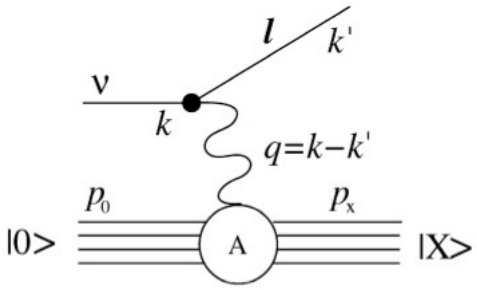

Figure 3.1: Diagrammatic representation of the process $\nu_\ell + A \to \ell^- + X$.

where the sum includes all hadronic final states. The calculation of $W_A^{\mu\nu}$ at moderate momentum transfer ($\mathbf{q} \lesssim 0.5$ GeV) can be carried out using non-relativistic wave functions to describe the initial and final states and expanding the current operator in powers of $\mathbf{q}/M$, M being the nucleon mass. However, at higher values of $|\mathbf{q}|$, corresponding to $E_\nu \gtrsim 1GeV$, the final states $|X\rangle$ can no longer be described in terms of non-relativistic nucleons only. Calculations of $W_A^{\mu\nu}$ in this regime require a set of simplifying assumptions, allowing one to take into account the relativistic motion of final state particles carrying momentum $\sim \mathbf{q}$, as well as the occurence of inelastic processes, leading to the appearance of hadrons other than protons and neutrons.

The Impulse Approximation (IA) scheme, which will be followed in this work, is based on the assumptions that, at large enough $\mathbf{q}$, the target nucleus is seen by the probe as a collection of individual nucleons and the interactions between the particles produced at the interaction vertex and the spectator nucleons can be neglected. A schematic representation of the IA cross section is given in Fig. 3.2.

Within the IA picture, the nuclear current can be written as a sum of one-body currents, i.e.

$$J_A^\mu \longrightarrow \sum_i j_i^\mu \ , \tag{3.39}$$

while the final state reduces to the direct product of the hadronic state produced at

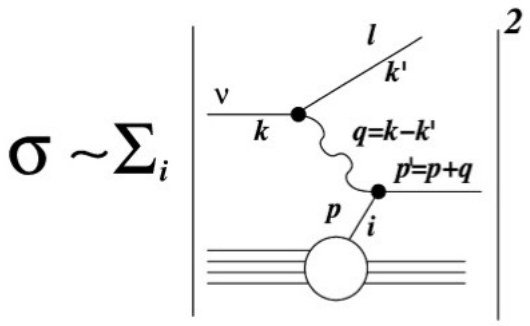

Figure 3.2: Schematic representation of the cross section of the process $\nu_\ell + A \to \ell^- + X$ in the IA scheme.

the interaction vertex, with momentum $\mathbf{p}'$, and the state describing the $(A-1)$-nucleon residual system, carrying momentum p_R, i.e.

$$|X\rangle \longrightarrow |i, p'\rangle \otimes |R, p_R\rangle \ , \tag{3.40}$$

implying that we can replace:

$$\sum_X |X\rangle\langle X| \to \sum_x \int d^3p_x |x, \mathbf{p}_x\rangle\langle \mathbf{p}_x, x| \sum_R d^3p_R |R, \mathbf{p}_R\rangle\langle \mathbf{p}_R, R| \ . \tag{3.41}$$

Moreover, the insertion of a complete set of free nucleon states, satisfying

$$\int d^3k |N, \mathbf{k}\rangle\langle \mathbf{k}, N| = 1, \tag{3.42}$$

leads to the factorization of the nuclear current matrix element according to

$$\langle 0|J_A^\mu|X\rangle = \Big(\frac{M}{\sqrt{|\mathbf{p}_R|^2 + M^2}}\Big)^{1/2} \langle 0|R, \mathbf{p}_R; N, -\mathbf{p}_R\rangle \sum_i \langle -\mathbf{p}_R, N|j_i^\mu|x, \mathbf{p}_x\rangle \ , \tag{3.43}$$

where the factor $E_{\mathbf{p}_R} = (M/\sqrt{|\mathbf{p}_R|^2 + M^2})^{1/2}$ takes into account the implicit covariant normalization of $\langle -\mathbf{p}_R, N|$ in the matrix element of j_i^μ.

Using the above relations, the hadronic tensor can be rewritten in the form

$$W^{\mu\nu} = \sum_{x,R} \int d^3p_R d^3p_x |\langle 0|R, \mathbf{p}_R; N, -\mathbf{p}_R\rangle|^2 \frac{M}{E_{\mathbf{p}_R}} \sum_i \langle -\mathbf{p}_R, N|j^{\mu\dagger}_i|x, \mathbf{p}_x\rangle\langle \mathbf{p}_x, x|j_i^\nu|N, -\mathbf{p}_R\rangle$$
$$\times \delta^3(\mathbf{q} - \mathbf{p}_R - \mathbf{p}_x)\delta(\omega + E_0 - E_R - E_X) \ , \tag{3.44}$$

where E_0 is the target ground state energy, $E_R = \sqrt{|\mathbf{p}_R|^2 + M_R^2}$, M_R being the mass of the recoiling system and E_X the energy of the final state X.

Using the identity

$$\delta(\omega + E_0 - E_R - E_X) = \int dE \delta(E - M + E_0 - E_R)\ \delta(\omega - E + M - E_X)\ , \tag{3.45}$$

we finally get

$$\begin{aligned} W_A^{\mu\nu} = &\sum_X \sum_R \int d^3p_X d^3p_R dE |\langle 0|R, \mathbf{p}_R; N, -\mathbf{p}_R\rangle|^2 \delta(E - M + E_0 - E_R)\delta^3(\mathbf{q} - \mathbf{p}_x - \mathbf{p}_R) \\ &\times \frac{M}{E_{\mathbf{p}_R}} \sum_i \langle -\mathbf{p}_R, N|j_i^\mu|X, \mathbf{p}_X\rangle\langle X, \mathbf{p}_X|j_i^\nu| - \mathbf{p}_R, N\rangle \delta(-E + M + \omega - E_X)\ . \end{aligned} \tag{3.46}$$

At this stage, we introduce the target spectral function $P(E, \mathbf{p})$, defined as

$$P(\mathbf{p}, E) = \sum_R |\langle 0|R, -\mathbf{p}\rangle|^2 \delta(E - M + E_0 - E_R) \tag{3.47}$$

expressing the probability distribution of finding a nucleon with momentum $\mathbf{p}$ and removal energy E in the target nucleus.[2].

Using Eq.(3.47), and the definition of the tensor describing the interactions of the i-th nucleon in free space (the subscript $\alpha = p\ n$ denotes protons and neutrons)

$$W_\alpha^{\mu\nu} = \sum_X \langle -\mathbf{p}_R, N|j^{\mu\dagger}_\alpha|X, \mathbf{p}_X\rangle\langle X, \mathbf{p}_X|j_\alpha^\nu| - \mathbf{p}_R, N\rangle \delta^{(4)}(p_N + \tilde{q} - p_X)\ . \tag{3.48}$$

the hadronic tensor can be written in the more concise form

$$W_A^{\mu\nu} = \int d^3p_X d^3p dE P(\mathbf{p}, E)\ \frac{M}{E_p}\left[Z W_p^{\mu\nu} + (A - Z) W_n^{\mu\nu}\right]\ , \tag{3.49}$$

Z being the nuclear charge. Note that in Eq.(3.48) we have introduced the quantity $\tilde{q}$, defined as

$$\tilde{q} = (\tilde{\omega}, q) \tag{3.50}$$

[2]We will make the simplifying assumption, fully justified in the case of isospin symmetric targets, that the proton and neutron spectral functions be the same.

with

$$\tilde{\omega} = E_X - \sqrt{\mathbf{p}^2 + M^2} = \omega + M - E - \sqrt{\mathbf{p}^2 + M^2} = \omega + E_0 - E_R - \sqrt{\mathbf{p}^2 + M^2} \ . \quad (3.51)$$

The replacement of ω with $\tilde{\omega}$ is meant to take into account the fact that a fraction $\delta\omega$ of the energy transfer goes into excitation energy of the spectator system. Therefore, the elementary scattering process can be described as if it took place in free space with energy transfer $\tilde{\omega} = \omega - \delta\omega$.

Using the tri-dimensional delta function to perform the integration on d^3p_X we finally get:

$$\begin{aligned} W_A^{\mu\nu} = & \int d^3p dE P(E,\mathbf{p}) \delta(\tilde{\omega} + \sqrt{\mathbf{p}^2 + M^2} - E_X) \\ & \times \frac{M}{E_p} \sum_X \langle \mathbf{p}, N | j_i^\mu | X, \mathbf{p} + \mathbf{q} \rangle \langle X, \mathbf{p} + \mathbf{q} | j_i^\nu | \mathbf{p}, N \rangle \ . \end{aligned} \quad (3.52)$$

In conclusion, within the IA scheme it is possible to trace back the hadronic tensor corresponding to the nuclear target to the one describing the elementary interaction with an isolated nucleon, provided q is replaced with $\tilde{q}$ and an integration on the nucleon momentum and removal energy is carried out, with a weight given by the spectral function.

Substituting the hadronic tensor into the definition of the cross section yields

$$\frac{d^2\sigma_{IA}}{d\Omega dE_l} = \int d^3p dE P(p,E) \frac{d^2\sigma_{elem}}{d\Omega dE_l}, \quad (3.53)$$

with

$$\frac{d^2\sigma_{elem}}{d\Omega dE_l} = \frac{G_F^2 V_{ud}^2}{16\pi^2} \frac{|\mathbf{p}'|}{|\mathbf{p}|} \frac{1}{4E_\mathbf{p} E_{\mathbf{p}+\mathbf{q}}} L_{\mu\nu} W^{\mu\nu} \ . \quad (3.54)$$

Equations (3.53) and (3.54) show that, within the IA, the theoretical calculation of the QE neutrino-nucleus cross section requires the knowledge of the nuclear spectral function and the nuclear form factors, determining the nuclear current. The boundaries of the integration region determining the ν-nucleus cross section are discussed in Appendix B.

Chapter 4

Confronting electron and neutrino scattering

As mentioned in Chapter 2, the analysis of the MiniBooNE data is carried out within the Relativistic Fermi Gas Model (RFGM). According to this model, the target nucleus is described as a collection of non interacting nucleons, bound with constant energy ϵ.

The wealth of information obtained from precise measurements of the electron-nucleus cross section in a broad kinematical domain have clearly exposed the limits of the description of nuclei based on the mean field approximation, of which the RFGM can be regarded as the crudest implementation. The combined analyses of inclusive and semi-inclusive data have shown that correlation effects suppress the occupation probability of the shell model states by about 20%, thus leading to the appearance of non vanishing cross sections well beyond the kinematical limits predicted by the mean field approach.

In this Chapter, after pointing out the limits of applicability of the RFGM, emerging from the analysis of electron scattering data, we will describe a dynamical model allowing one to construct the nuclear spectral functions taking into account the effects of nucleon-nucleon correlations. In Section 4.2, we will show the results of theoretical calculations of the electron- and neutrino- carbon cross section, and point out the difficulties arising from the flux average, hindering the identification of the dominant reaction mechanism.

4.1 Realistic models of the nuclear spectral function

According to the RFGM, the nuclear spectral function, defined in Eq. (3.47), can be written in the simple form:

$$P_{RFGM}(p,E) = \frac{6\pi^2 A}{p_F^3}\ \theta(p_F - p)\ \delta(E_p - \epsilon + E) \tag{4.1}$$

where p_F is the Fermi momentum and ϵ is the average binging energy, introduced to account for nuclear binding. The term in parenthesis is a constant needed to normalize the spectral function to the number of target nucleons, A. The values of the two parameters, ϵ and p_F, are determined by fitting position and width of the quasi elastic peak of the measured electron-nucleus scattering cross sections.

Electron scattering data have provided overwhelming evidence that the energy-momentum distribution of nucleons in the nucleus is quite different from the one predicted by the RFGM. This is to be ascribed to the presence of nucleon-nucleon (NN) correlations, mainly arising from the strongly repulsive nature of the NN interaction at short distances.

The most prominent evidence of the presence of a strongly repulsive core is provided by the saturation of the observed nuclear charge densities with increasing A. Figure4.1 clearly shows that the charge density in the nucleus interior is in fact independent of A for A $\geq$ 16.

Dynamical correlations give rise to virtual scattering processes leading to the excitation of the partecipating nucleons to states of energy larger than the Fermi energy, thus depleting the single particle levels within the Fermi sea. Owing to the contribution of nucleons belonging to a correlated pair, the nuclear spectral function $P(\mathbf{p}, E)$ extends to the region $|p| \gg p_F$ and $E \gg \epsilon$.

The target spectral function, needed to compute the nuclear cross section within the IA, is given by Eq. (3.47). Its definition involves the A-nucleon ground state, as well as the full spectrum of the (A - 1)-nucleon system. Within the framework of Nuclear Many

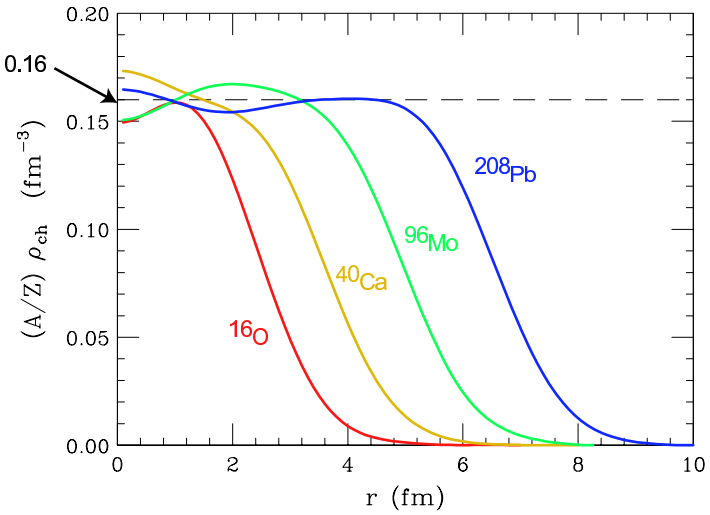

Figure 4.1: Radial dependence of nuclear charge-distributions measured by elastic electron scattering.

Body Theory (NMBT), these states are obtained solving the Schrödinger equation with the Hamiltonian:

$$H = \sum_{i=1}^{A} \frac{p_i^2}{2m} + \sum_{j>i=1}^{A} v_{ij} + \ldots, \tag{4.2}$$

where p_i is the momentum of the i-th nucleon, v_{ij} describes two-nucleon interactions and the ellipses refer to the presence of additional terms describing interactions involving three or more nucleons. The nucleon-nucleon (NN) potential, which reduces to the Yukawa one-pion exchange potential at large internucleon distance, is obtained from an accurate fit to the available data on the two-nucleon system, i.e. deuteron properties and ~ 4000 NN precisely measured scattering phase shift, at energies up to pion production threshold.

The calculation of the spectral function, $P(\mathbf{p}, E)$, within NMBT involves a degree of complexity that rapidly increases with A. For this reason, so far it has been only carried out for $A \leq 4$. However, thanks to the simplifications associated with translation invariance, highly accurate results are also available for uniform nuclear matter, i.e. in the limit $A \to \infty$ with Z= A/2 (Z denotes the number of protons). The proton spectral functions

of nuclei with $A > 4$ have been modeled using the local density approximation (LDA), in which the experimental information obtained from nucleon knock-out measurements is combined with theoretical calculations of nuclear matter at different densities.

Within the LDA scheme, the spectral function is written in the form [17]

$$P_{LDA}(\mathbf{p}, E) = P_{MF}(\mathbf{p}, E) + P_{corr}(\mathbf{p}, E) \ , \tag{4.3}$$

where the two terms describe the contributions arising from the nuclear mean field and NN correlations, respectively. The former can be extracted from the available semi inclusive, $(e, e'p)$ data, and is usually written in the factorized form:

$$P_{MF}(\mathbf{p}, E) = \sum_{n \in \{F\}} Z_n |\phi_n(\mathbf{p})|^2 F_n(E - E_n) \ , \tag{4.4}$$

where the spectroscopic factor $Z_n < 1$ and the function $F_n(E - E_n)$, describing the energy width of the n-th state, accounts for the effects of residual interactions not included in the mean-field picture. In the absence of these residual interactions, $Z_n \rightarrow 1$ and $F(E - E_n) \rightarrow \delta(E - E_n)$.

In a nucleus of mass number A is, the correlation contribution is given by

$$P_{corr}(\mathbf{p}, E) = \int d^3r \varrho_A(\mathbf{r}) P^{NM}_{corr}(\mathbf{p}, E; \varrho = \varrho_A(\mathbf{r})) \ , \tag{4.5}$$

where $\varrho_A(\mathbf{r})$ is the nuclear density distribution and $P^{NM}_{corr}(\mathbf{p}, E; \varrho)$ is the correlation part of the spectral function of uniform nuclear matter at density ϱ.

Note that the spectroscopic factors Z_n are constrained by the normalization requirement

$$\int d^3p dE P_{LDA}(\mathbf{p}, E) = 1. \tag{4.6}$$

The LDA scheme is based on the assumption that short-range nuclear dynamics are unaffected by surface and shell effects. The validity of this assumption is supported by the results of theoretical calculations of the nucleon momentum distribution

$$n(\mathbf{p}) = \int dE P(\mathbf{p}, E) \tag{4.7}$$

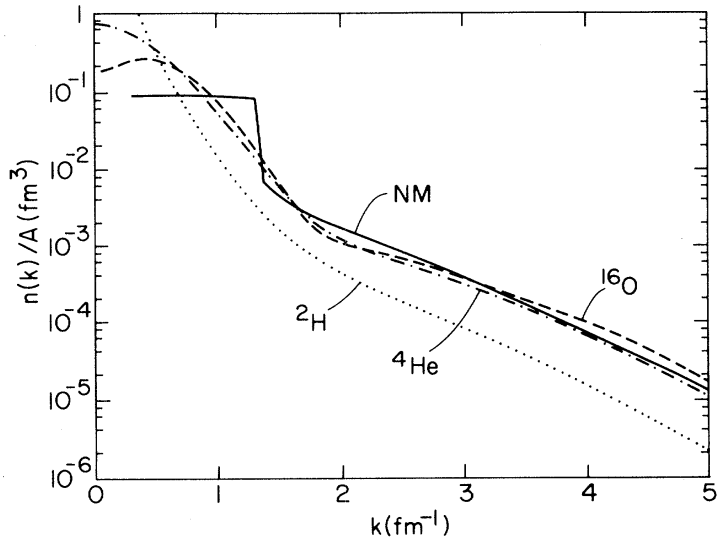

Figure 4.2: Calculated momentum distribution per nucleon in $2H$,[4] He,[16] O, and uniform nuclear matter (NM).

showing that for $A \geq 4$ the quantity $n(\mathbf{p})/A$ becomes nearly independent of A at large $|\mathbf{p}|(\gtrsim 350$ MeV). This feature, illustrated in Fig. 4.2 suggests that the correlation part of the spectral function also scales with the target mass number.

The oxygen spectral function obtained in Ref. [18] within the LDA approach is shown in Fig. 4.3. For comparison, in Fig. 4.4 we also show the momentum distribution obtained from the spectral function of Fig. 4.3, the RFGM, and a Monte Carlo simulation carried out using an highly realistic wave function [19].

4.2 Comparison to electron and neutrino-carbon scattering data

Using the LDA carbon spectral function and the vector and axial currents discussed in Chapter 3, one can compute the inclusive electron- and neutrino-nucleus cross sections, that can both be expressed as in Eq.(3.53) with the appropriate elementary cross sections.

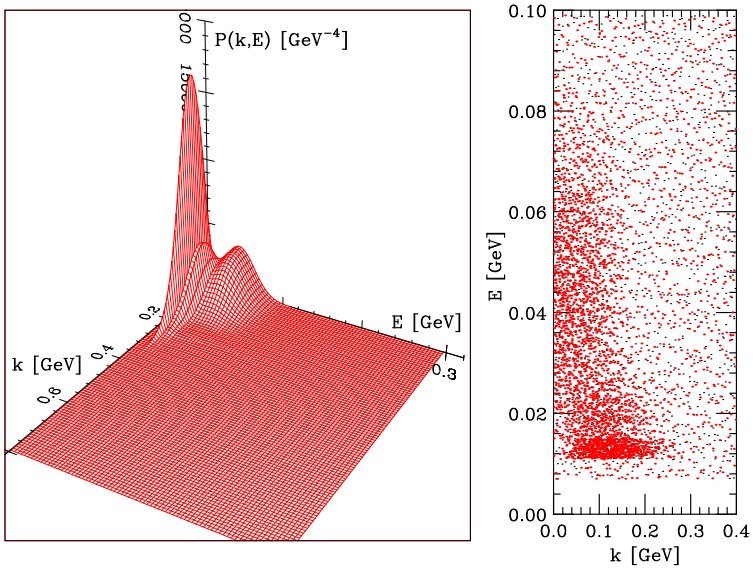

Figure 4.3: Oxygen spectral function obtained within the LDA approximation [18].

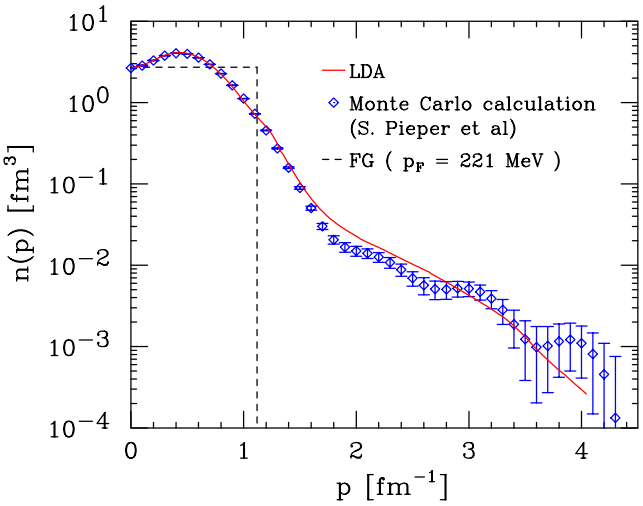

Figure 4.4: Comparison between the momentum distribution obtained from the spectral function of Ref. [18] (see Fig. 4.3), the RFGM, and a Monte Carlo simulation carried out using a realistic wave function [19].

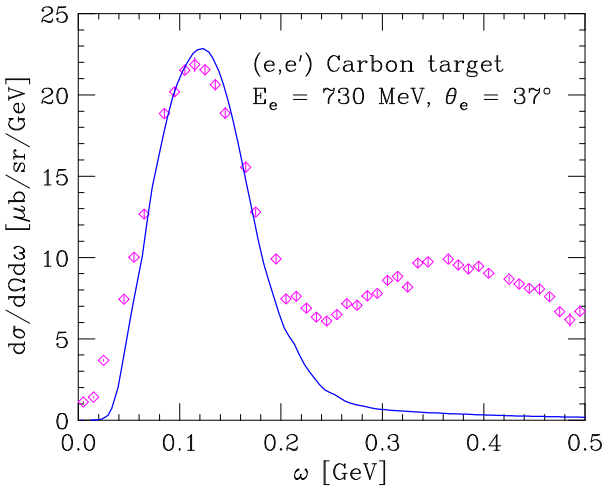

Figure 4.5: Quasi elastic electron-carbon cross section, obtained using the spectral function of Ref.[17] and the vector form factors of Ref.[13], plotted as a function of the energy loss ω. The data points are taken from Ref. [20].

Figure 4.5 shows the results of a theoretical calculation of the quasi elastic electron scattering cross section off carbon, at beam energy $E_e = 730$MeV and electron-scattering angle $\theta_e = 37°$, plotted as a function of the energy loss ω.

It is apparent that height, position and width of the quasi elastic peak, mostly driven by the energy and momentum dependence of the hole spectral function, are well reproduced.

Applying the same formalism to neutrino scattering leads to the results displayed in Fig. 4.6. The data points represent the double-differential CCQE cross section averaged over the MiniBooNE neutrino flux, whose mean energy is $\langle E_\nu \rangle = 788$ MeV, plotted as a function of the kinetic energy of the outgoing muon at different values of the muon scattering angle. The solid lines show the results (integrated over the $\cos\theta_\mu$ bins) obtained using the same spectral functions and vector form factors employed in the calculation of the electron-scattering cross-section of Fig. 4.5, and a dipole parametrization of the axial form

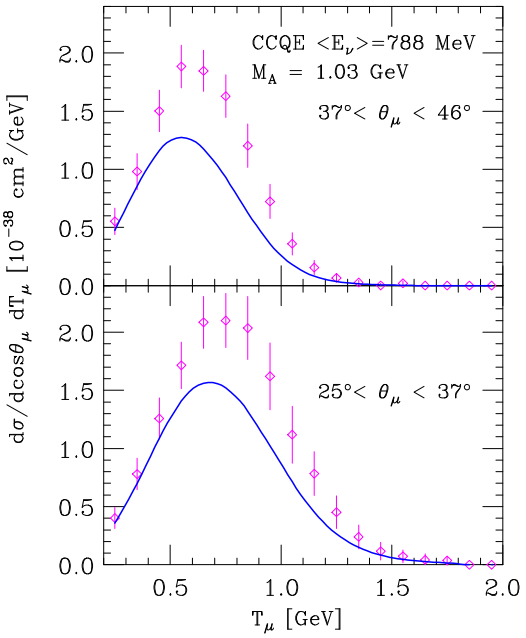

Figure 4.6: Flux averaged double differential CCQE cross section measured by the MiniBooNE collaboration, shown as a function of the kinetic energy of the outgoing muon. The upper and lower panels correspond to different values of the muon scattering angle. The theoretical calculations have been carried out using the spectral function of Ref. [17], the vector form factors of Ref. [13] and a dipole parametrization of the axial form factor with $M_A = 1.03$ GeV.

factor with $M_A = 1.03$ GeV. Comparison of Figs. 4.5 and 4.6 indicates that the electron and neutrino cross sections corresponding to the same target and comparable kinematical conditions (the position of the QE peak in Fig. 4.5 corresponds to kinetic energy of the scattered electron $\sim$ 610 MeV) cannot be explained by using the same theoretical approach and the value of the axial mass resulting from deuterium measurements.

As already mentioned, the first explanation put forward to explain the MiniBooNE CCQE cross sections was based on the suggestion that the value of M_A may be modified in the nuclear medium. On the other hand, electron scattering data have provide strong evidence that the vector form factors are *not* modified.

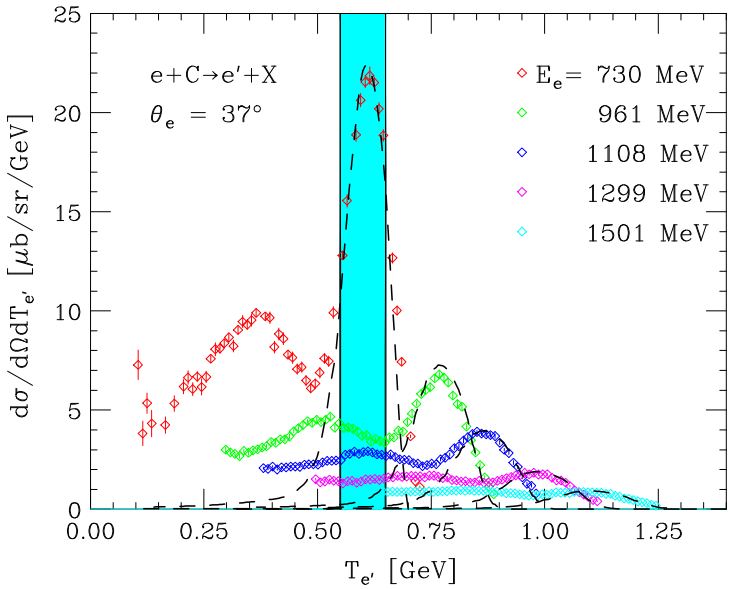

Figure 4.7: Inclusive electron-carbon cross sections at $\theta_e = 37^o$ and beam energies ranging between 0.730 and 1.501 GeV. The dashed lines represents the single nucleon knock out contribution. The shaded area shows the energy bin corresponding to the peak of the cross section of Fig. 4.5. The data are taken from Refs. [20, 22].

In Refs. [10, 21] it is argued that the excess strength may instead be explained by the fact that, owing to the flux average, the experimental cross sections shown in Fig.4.6 include contributions of events other than CCQE.

The implications of flux average can be easily understood considering the neutrino cross section at muon energy corresponding to the maximum of the spectrum shown in the upper panel of Fig. 4.7, i.e. $T_\mu = 0.55$ GeV, and $\cos\theta = 0.75$. In this kinematics, Bjorken $x = 1$, corresponding to the quasi elastic peak, and $x = 0.5$, corresponding to the dip region between the quasi elastic peak and the Δ-production peak (see Fig. 1) are associated with neutrino energy $E_\nu = 0.778$ and 0.975 GeV, respectively. As the values of the MiniBooNE flux corresponding to these energies are within less than 20% of one another, flux integration leads to collect contributions from different regimes, in which

different reaction mechanisms are expected to dominate, with about the same probability.

This feature can be best illustrated using the measured electron-carbon scattering cross sections. Figure 4.7 shows the data from Refs. [20, 22], taken at electron scattering angle $\theta_e = 37^\circ$ and beam energies ranging between 0.730 and 1.501 GeV, plotted as a function of the energy of the outgoing electron. It clearly appears that the energy bin corresponding to the top of the quasi elastic peak at $E_e = 0.730$ GeV, shown by the shaded area, receives significant contributions from cross sections corresponding to different beam energies and different values of x. As a consequence, the description of the flux-integrated CCQE neutrino nucleus cross section is likely to require the inclusion of reaction mechanisms other than single nucleon knockout. Assuming that processes involving pion-production be properly identified, the most important competing mechanism is multi-nucleon knockout, leading to two particle-two hole (2p2h) final states. Note that in the MiniBooNE analysis (see Chapter 2) these final states cannot be distinguished from the one particle-one hole final states associated with single nucleon knockout.

Multinucleon knockout is known to occur due to:

- NN correlations in the initial state;
- final state interactions between the struck nucleon and the spectator particles;
- coupling to the two-body nuclear electroweak current.

As we already pointed out, the effect of NN correlations is taken into account in the LDA spectral function. It gives rise to the tail extending to large ω, clearly visible in Fig. 4.5. On the other hand, the available estimates suggest that in the MiniBooNE kinematical setup final state interactions cannot explain the reported excess of CCQE events. The most important correction is likely to arise from processes involving the nuclear two-body current, the inclusion of which is long known to be needed to explain the nuclear electromagnetic response in the transverse channel.

Chapter 5

Contribution of the two-nucleon current operator

In this Chapter we will discuss meson-exchange currents (MEC), and their contribution to the nuclear cross sections. Meson exchange is known to be the mechanism driving NN interactions at large and intermediate distances. However, it should be kept in mind that the description in terms of meson exchange is only justified at energies below the meson production threshold. At higher energies the non-nucleonic degrees of freedom have to be explicitly taken into account.

As a first step, we shall limit ourselves to a preliminary analysis, in which electromagnetic interactions and pion exchange are considered. After analyzing the structure of the main contributions to the two-nucleon current and the problems arising from the requirement of gauge invariance, we will derive the expression of the nuclear cross section including one- and two-body currents. In order to keep the formalism as light as possible, we will consider a deuterium target.

5.1 The nuclear electroweak current operator

Most calculations of MEC contributions to the electron and neutrino scattering cross section have been carried out expanding the current operator in powers of $|\mathbf{q}|/M$ [23].

The resulting nuclear electromagnetic and axial current operators are written as a sum of one-, two-, and many-body terms, depending on the degrees of freedom of an increasing number nucleons:

$$j^0(q) = \varrho(q) = \sum_i \varrho_i^{(1)}(q) + \sum_{i<j} \varrho_{ij}^{(2)}(q) + \dots \ , \tag{5.1}$$

$$\mathbf{j}(q) = \sum_i \mathbf{j}_i^{(1)}(q) + \sum_{i<j} \mathbf{j}_{ij}^{(2)}(q) + \dots \ , \tag{5.2}$$

$$\mathbf{A}_a(q) = \sum_i \mathbf{A}_{a,i}^{(1)}(q) + \sum_{i<j} \mathbf{A}_{a,ij}^{(2)}(q) + \dots \ . \tag{5.3}$$

The one-body operators $\varrho_i^{(1)}$ and $\mathbf{j}_i^{(1)}$ are obtained from the covariant single-nucleon current:

$$j^\mu = \bar{u}(p')\Big[F_V(Q^2)\gamma^\mu + F_M(Q^2)\frac{i\sigma^{\mu\nu}q_\nu}{2m}\Big]u(p) \tag{5.4}$$

whose expression is discussed in both Chapter 3 and Appendix A, while the one-body contribution to the axial current is obtained from:

$$A_a^\mu = \bar{u}(p')\Big[F_A(Q^2)\gamma^\mu + F_P(Q^2)q^\mu\Big]\gamma_5\frac{\tau_a}{2}u(p) \ . \tag{5.5}$$

The Q^2 dependence of F_A is given by Eq.(2.6), while the induced pseudoscalar form factor is parametrized in the form $F_P(Q^2) = G_P(Q^2)/2M$, with

$$G_P(Q^2) = \frac{g_{\pi NN}(Q^2)}{g_{\pi NN}(0)}\frac{G_P(0)}{1+Q^2/m_\pi^2} \ , \tag{5.6}$$

$g_{\pi NN}(Q^2)$ being the πNN strong-interaction form factor.

In this work, we will use a fully relativistic expression of the electromagnetic two-body current, to be discussed in the next section.

Before, switching to electromagnetic interactions, in Fig. 5.1 we show the total CCQE neutrino-deuteron cross section obtained using Eq.(3.37) and the deuteron wave function described in Appendix C, and including one-body currents only. The axial form factor has been assumed to exhibit a dipole Q^2-dependence, with an axial mass $M_A = 1.03$ GeV.

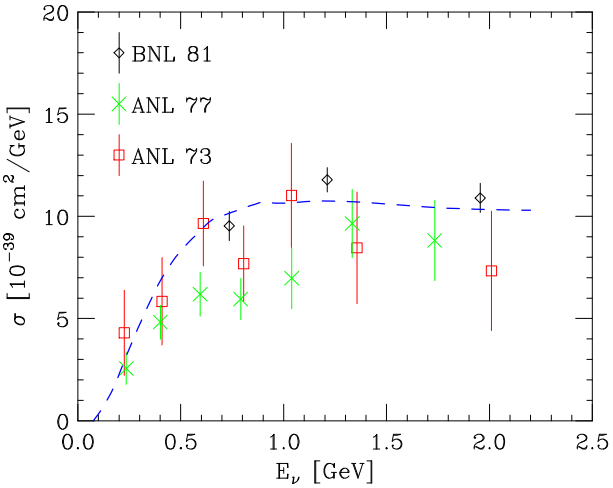

Figure 5.1: CCQE neutrino-deuteron total cross section as a function of neutrino energy. The theoretical results have been obtained using Eq.(3.37), the deuteron wave function described in Appendix C and the nculeon axial mass $M_A = 1.03$ GeV. The experimental data are from Refs. [24, 25, 26].

It is apparent that, as discussed in Chapter 2, within the limited statistics of deuteron experiments the data is compatible with this value of M_A.

5.2 Electromagnetic two-body current operator

At intermediate and large inter nucleon separation distances, NN interactions are known to be due to π- and ϱ-meson exchanges. Here we will focus only on processes mediated by pions.

Before defining the interaction Lagrangians, it is useful to specify our notation. The isospin triplet of pion fields $\pi_a(x)$ with $a = 1, 2, 3$ is written in the form

$$\pi_a = \sum_p \frac{1}{2\omega_p} \left[c_{p,a} e^{ipx} + \text{h.c.} \right] , \tag{5.7}$$

where the annihilation and creation operators, $c_{p,a}$ and $c^\dagger_{p,a}$, satisfy standard commutation relations, and $\omega_p \equiv (p^2 + m_\pi^2)^{1/2}$.

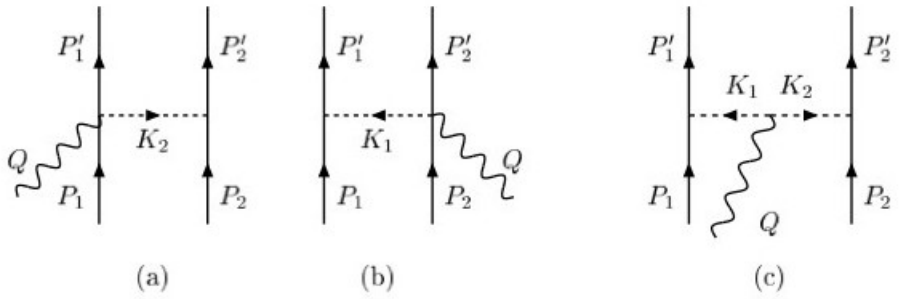

Figure 5.2: Feynmann diagrams describing the two-body current associated with one-pion exchange.

The non-interacting Lagrangian is given by

$$L_\pi = \frac{1}{2}\partial_\mu \pi_a \partial^\mu \pi_a - \frac{1}{2} m_\pi^2 \pi_a \pi_a \ . \tag{5.8}$$

To simplify the notation, in the following we will denote $L_{\rm mass} = -\frac{1}{2} m_\pi^2 \pi_a \pi_a$, in the derivation of the interaction terms. The first step consists of introducing the charged pion fields

$$\pi^+ = \frac{\pi_1 + i\pi_2}{\sqrt{2}}, \qquad \pi^- = \frac{\pi_1 - i\pi_2}{\sqrt{2}}. \tag{5.9}$$

Substitution of the above definitions in Eq.(5.8) leads to

$$L_\pi = \left(\partial_\mu \frac{\pi_1 + i\pi_2}{\sqrt{2}}\right)^* \left(\partial^\mu \frac{\pi_1 + i\pi_2}{\sqrt{2}}\right) + \frac{1}{2}\partial_\mu \pi_3 \partial^\mu \pi_3 + L_{\rm mass} \ . \tag{5.10}$$

We now include electromagnetic interactions of charged pions through minimal substitution, i.e. replacing

$$\partial_\mu \pi_\mp \longrightarrow \left[(\partial_\mu \mp ieA_\mu)\pi_\mp\right] \ . \tag{5.11}$$

Neglecting terms quadratic in the electromagnetic field, this procedure yields

$$\begin{aligned} L_\pi &= (\partial_\mu - ieA_\mu)\frac{(\pi_1 - i\pi_2)}{\sqrt{2}}(\partial^\mu + ieA^\mu)\frac{(\pi_1 + i\pi_2)}{\sqrt{2}} + \frac{1}{2}\partial_\mu \pi_3 \partial^\mu \pi_3 + L_{\rm mass} \\ &= \frac{1}{2}\partial_\mu \pi_1 \partial^\mu \pi_1 + \frac{1}{2}\partial_\mu \pi_2 \partial^\mu \pi_2 + \frac{1}{2}\partial_\mu \pi_3 \partial^\mu \pi_3 + eA_\mu(\pi_1 \partial^\mu \pi_2 - \pi_2 \partial^\mu \pi_1) + L_{\rm mass} \ . \end{aligned} \tag{5.12}$$

It is worth noting the appearance of the term

$$L_{\pi\pi\gamma} = eA_\mu(\pi_1\partial^\mu\pi_2 - \pi_2\partial^\mu\pi_1) \ , \tag{5.13}$$

describing the interaction between two π-mesons and a γ.

On he other hand, the Lagrangian describing the interaction vertex involving two nucleons and a π can be written, assuming pseudovector πNN coupling, as

$$L_{\pi NN} = \frac{f}{m_\pi}\bar{N}\gamma_5\gamma^\mu(\partial_\mu\pi_a)\tau_a N \ , \tag{5.14}$$

where

$$N = \begin{pmatrix} p \\ n \end{pmatrix} \ , \tag{5.15}$$

is a isospin doublet describing the nucleon field, and f denotes the πNN coupling constant.

The electromagnetic currents corresponding to diagrams (a)-(c) of Fig. 5.2 are obtained by computing the S-matrix element:

$$S_{fi} = S_{fi}(P_1', P_2', P_1, P_2) - S_{fi}(P_1', P_2', P_2, P_1) \tag{5.16}$$

for the absorption of a virtual photon by a system of two nucleons, namely for the process:

$$\gamma + N_1 + N_2 \longrightarrow N_1' + N_2' \tag{5.17}$$

with $P_1, P_2(P_1', P_2')$ being the initial (final) four-momenta of the two participating nucleons.

The electromagnetic current is then defined according to

$$S_{fi}(P_1', P_2', P_1, P_2) = -ieA_\mu(Q)2\pi\delta(E_1' + E_2' - E_1 - E_2 - \omega)\langle P_1'P_2'|j^\mu(Q)|P_1P_2\rangle. \tag{5.18}$$

where $A_\mu(Q)$ is related to the matrix element of the electromagnetic field between the state describing the incident photon with momentum Q and the vacuum state, namely

$$\langle 0|A_\mu(X)|\gamma(Q)\rangle = A_\mu(Q)e^{-iQ\cdot X}. \tag{5.19}$$

Finally, the on-shell matrix element of the two-body current can be written in terms of a function $j^\mu(p_1', p_2', p_1, p_2)$ as follows:

$$\begin{aligned}&\langle P_1' P_2' | j^\mu(Q) | P_1, P_2 \rangle \\ &\quad = (2\pi)^3 \delta^{(3)}(p_1' + p_2' - q - p_1 - p_2) \frac{M^2}{V^2 (E_{p_1} E_{p_2} E_{p_1'} E_{p_2'})^{1/2}} j^\mu(p_1', p_2', p_1, p_2),\end{aligned} \tag{5.20}$$

where M is the nucleon mass, V is the normalization volume and $E_p = \sqrt{p^2 + M^2}$ the on-shell energy of a nucleon with momentum p.

We now begin analyzing diagram (c), as we have all the tools needed to derive the pion-in-flight current matrix element (isospin summation is understood). We obtain

$$\begin{aligned}j_p^\mu(p_1', p_2'; p_1, p_2) =& \frac{f^2}{m_\pi^2} \bar{N}(p_1') \gamma_5 \gamma^\mu(k_\mu^1) \tau^{(+)} N(p_1) \Big(\frac{1}{k_1^2 - m_\pi^2} \Big) \\ & \times \frac{F_\pi}{2} (k_1 - k_2)^\mu \Big(\frac{1}{k_2^2 - m_\pi^2} \Big) \; \bar{N}(p_2') \gamma_5 \gamma^\nu (-i k_\nu^2) \tau^{(-)} N(p_1) \; ,\end{aligned} \tag{5.21}$$

yielding

$$j_p^\mu = \frac{p^2}{m_\pi^2} i \epsilon_{3ab} \tau_a \tau_b \bar{N}(p_1') \gamma_5 \not{k}_1 N(p_1) \frac{F_\pi (k_1 - k_2)^\mu}{(k_1^2 - m_\pi^2)(k_2^2 - m_\pi^2)} \bar{N}(p_2') \gamma_5 \not{k}_2 N(p_2) \; . \tag{5.22}$$

The contributions associated with the Feynman diagrams (a)-(b) in Fig. 5.2, corresponding to the so called seagull (or contact) current matrix element, are given by

$$j_s^\mu = \frac{f^2}{m_\pi^2} i \epsilon_{3ab} \bar{N}(p_1') \tau_a \gamma_5 \not{k}_1 N(p_1) \frac{F_1^V}{k_1^2 - m_\pi^2} \bar{N}(p_2') \tau_b \gamma_5 \gamma^\mu N(p_2) + (1 \to 2) \; . \tag{5.23}$$

In the above equation, k_1 and k_2 are the four momenta given to nucleons 1 and 2, as illustrated in Fig. 5.2, while F_V^1 and F_π are the electromagnetic isovector nucleon and pion form factor, respectively.

The electromagnetic current must obey the continuity equation:

$$\partial_\mu j^\mu = 0 \; , \tag{5.24}$$

implying

$$\boldsymbol{\nabla} \cdot \boldsymbol{j} + i[H, j^0] = 0 \; . \tag{5.25}$$

The currents defined in Eqs.(5.22) and (5.23), commute with the one-pion exchange potential by construction. However, realistic nuclear hamiltonians involve phenomenological potentials exhibiting a more complex structure (see Chapter 3). A procedure to generalize Eqs.(5.22) and (5.23), to make them consistent with the requirement of current conservation, has been developed in Refs.[27, 28]. However, in this exploratory study we will restrict ourselves to the pion-exchange currents defined on in Eqs.(5.22) and (5.23).

5.3 Electron-deuteron cross section

In Born approximation, the differential cross section of the process $e + {}^2\mathrm{H} \to e + X$, can be written in the form (compare to Eq. (3.37)):

$$\frac{d^2\sigma}{d\Omega_{e'} dE_{e'}} = \frac{\alpha^2}{Q^4} \frac{E_{e'}}{E_e} L_{\mu\nu} W^{\mu\nu} \tag{5.26}$$

where E_e is the energy of the incident beam and $E_{e'}$ is the energy of the outgoing electron in the final state while. The tensor $L_{\mu\nu}$ is the symmetric part of the leptonic tensor defined in Eq.(3.14), while

$$W^{\mu\nu} = \frac{1}{2s+1} \sum_{M_s} \sum_{x} \langle 0|J^\mu|x\rangle\langle x|J^\nu|0\rangle \delta^{(4)}(p_0 + q - p_x) \ , \tag{5.27}$$

where p_0 and p_x are the four-momenta of the initial and final hadronic states, respectively, while s and M_s denote the target spin and its projection along the quantization axis.

The nuclear current, involving both one- and two-body contributions, can be written in the form

$$\langle \mathbf{x}_1\mathbf{x}_2|J^\mu|\mathbf{x}_1\mathbf{x}_2\rangle = J_1^\mu(\mathbf{x}_1) + J_1^\mu(\mathbf{x}_2) + J_2^\mu(\mathbf{x}_1,\mathbf{x}_2) = J^\mu(\mathbf{x}_1,\mathbf{x}_2) \ , \tag{5.28}$$

impying that transformation to momentum space yields

$$\begin{aligned} J^\mu(\mathbf{q}_1,\mathbf{q}_2) &= \int d^3x_1 d^3x_2 e^{-i(\mathbf{q}_1\mathbf{x}_1 + \mathbf{q}_2\mathbf{x}_2)} J^\mu(\mathbf{x}_1,\mathbf{x}_2) \\ &= J_1^\mu(\mathbf{q}_1)(2\pi)^3\delta^{(3)}(\mathbf{q}_2) + J_2^\mu(\mathbf{q}_2)(2\pi)^3\delta^{(3)}(\mathbf{q}_1) + J_2^\mu(\mathbf{q}_1,\mathbf{q}_2) \ . \end{aligned} \tag{5.29}$$

The initial and final states are defined as

$$\langle x_1 x_2|0\rangle = \psi(\mathbf{x}_1,\mathbf{x}_2)|1\ M\rangle|0\ 0\rangle\ , \tag{5.30}$$

where $|1\ M\rangle$ and $|0\ 0\rangle$ refer to spin and isospin states, respectively, and

$$\langle x_1 x_2|x\rangle = \langle \mathbf{x}_1|\mathbf{p}_1\rangle\langle \mathbf{x}_2|\mathbf{p}_2\rangle\ |s_1 s_2\rangle|t_1 t_2\rangle\ , \tag{5.31}$$

$s_1 t_1$ and $s_2 t_2$ being the spin-isospin quantum numbers of the two final state nucleons, carrying momenta $\mathbf{p}_1$ and $\mathbf{p}_2$.

From Eq.(5.31) it follows that in Eq.(5.27) we can replace

$$\sum_x \longrightarrow \sum_{s_1 s_2}\sum_{t_1 t_2}\int \frac{d^3p_1}{(2\pi)^3}\frac{d^3p_2}{(2\pi)^3}\ , \tag{5.32}$$

obtaining

$$\begin{aligned} W^{\mu\nu} =& \frac{1}{3}\sum_M\sum_{s_1 s_2}\sum_{t_1 t_2}\int \frac{d^3p_1}{(2\pi)^3}\frac{d^3p_2}{(2\pi)^3}\delta^{(4)}(p_0+q-p_X) \\ & \times \langle 0|J^\mu|\mathbf{p}_1 s_1 t_1, \mathbf{p}_2 s_2 t_2\rangle\langle \mathbf{p}_1 s_1 t_1, \mathbf{p}_2 s_2 t_2|J^\nu|0\rangle. \end{aligned} \tag{5.33}$$

Let us now consider the matrix element of the nuclear current operator. Inserting a cmplete set of two-nucleon states $|\mathbf{k}_1\sigma_1\tau_1, \mathbf{k}_2\sigma_2\tau_2\rangle$ it can be rewritten in the form:

$$\begin{aligned} \langle \mathbf{p}_1 s_1 t_1, \mathbf{p}_2 s_2 t_2|J^\nu|0\rangle =& \sum_{\sigma_1\sigma_2}\sum_{\tau_1\tau_2}\int \frac{d^3k_1}{(2\pi)^3}\frac{d^3k_2}{(2\pi)^3} \\ & \times \langle \mathbf{p}_1 s_1 t_1, \mathbf{p}_2 s_2 t_2|J^\nu|\mathbf{k}_1\sigma_1\tau_1, \mathbf{k}_2\sigma_2\tau_2\rangle\Big(\frac{m}{E_{k_1}}\Big)^{1/2}\Big(\frac{m}{E_{k_2}}\Big)^{1/2}\langle \mathbf{k}_1\sigma_1\tau_1, \mathbf{k}_2\sigma_2\tau_2|0\rangle\ , \end{aligned} \tag{5.34}$$

where $E_k = (|\mathbf{k}|^2 + M^2)^{1/2}$ and

$$\langle \mathbf{k}_1\sigma_1\tau_1, \mathbf{k}_2\sigma_2\tau_2|0\rangle = \int d^3x_1 d^3x_2 \langle \mathbf{k}_1|\mathbf{x}_1\rangle\langle \mathbf{k}_2|\mathbf{x}_2\rangle\psi(\mathbf{x}_1,\mathbf{x}_2)\langle \sigma_1\sigma_2|1M\rangle\langle \tau_1\tau_2|0\ 0\rangle\ . \tag{5.35}$$

Let us now introduce center of mass and relative coordinates, in both position and momentum space

$$\boldsymbol{X} = \frac{\boldsymbol{x}_1+\boldsymbol{x}_2}{2}\quad ,\quad \boldsymbol{x} = \boldsymbol{x}_1 - \boldsymbol{x}_2\ , \tag{5.36}$$

$$\boldsymbol{K} = \boldsymbol{k}_1 + \boldsymbol{k}_2\quad ,\quad \mathbf{k} = \frac{\boldsymbol{k}_1 - \boldsymbol{k}_2}{2}\ , \tag{5.37}$$

in terms of which we can write the deuteron wave function

$$\psi(\mathbf{x}_1, \mathbf{x}_2) = e^{i\mathbf{K}_{CM}\cdot\mathbf{X}}\psi(\mathbf{x}) \longrightarrow \psi(\mathbf{x}) \tag{5.38}$$

where we have chosen to work in the laboratory frame, which amounts to setting $\mathbf{K}_{CM} = 0$.

Therefore, we find:

$$\begin{aligned}\langle \mathbf{k}_1\sigma_1\tau_1, \mathbf{k}_2\sigma_2\tau_2|0\rangle &= (2\pi)^3\delta^{(3)}(\mathbf{k}_1 + \mathbf{k}_2) \\ &\times \int d^3x e^{i(\mathbf{k}_1-\mathbf{k}_2)\mathbf{x}/2}\psi(\mathbf{x})\langle\sigma_1\sigma_2|1M\rangle\langle\tau_1\tau_2|0\ 0\rangle\ ,\end{aligned} \tag{5.39}$$

and substitution in Eq.(5.34) yields

$$\begin{aligned}\langle \mathbf{p}_1 s_1 t_1, \mathbf{p}_2 s_2 t_2|J^\nu|0\rangle &= \sum_{\sigma_1\sigma_2}\sum_{\tau_1\tau_2}\int \frac{d^3k_1}{(2\pi)^3}\frac{d^3k_2}{(2\pi)^3}\Big(\frac{m}{E_{k_1}}\Big)^{1/2}\Big(\frac{m}{E_{k_2}}\Big)^{1/2}(2\pi)^3\delta^{(3)}(\mathbf{k}_1+\mathbf{k}_2) \\ &\times \tilde{\psi}\Big(\frac{\mathbf{k}_1-\mathbf{k}_2}{2}\Big)\langle \mathbf{p}_1 s_1 t_1, \mathbf{p}_2 s_2 t_2|J^\nu|\mathbf{k}_1\sigma_1\tau_1, \mathbf{k}_2\sigma_2\tau_2\rangle\langle\sigma_1\sigma_2|1M\rangle\langle\tau_1\tau_2|0\ 0\rangle\ ,\end{aligned} \tag{5.40}$$

i.e.

$$\begin{aligned}\langle \mathbf{p}_1 s_1 t_1, \mathbf{p}_2 s_2 t_2|J^\nu|0\rangle &= \sum_{\sigma_1\sigma_2}\sum_{\tau_1\tau_2}\int \frac{d^3k}{(2\pi)^3}\Big(\frac{m}{E_k}\Big)\tilde{\psi}(k) \\ &\langle \mathbf{p}_1 s_1 t_1, \mathbf{p}_2 s_2 t_2|J^\nu|\mathbf{k}_1\sigma_1\tau_1, \mathbf{k}_2\sigma_2\tau_2\rangle\langle\sigma_1\sigma_2|1M\rangle\langle\tau_1\tau_2|0\ 0\rangle\ ,\end{aligned} \tag{5.41}$$

$\tilde{\psi}(k)$ being the deuteron wave function in momentum space.

We now rewrite the current in terms of its Fourier transform, using again center-of.mass and relative coordinates:

$$\begin{aligned}\mathbf{Q} &= \mathbf{q}_1 + \mathbf{q}_2 \quad , \quad \boldsymbol{\xi} = \frac{\mathbf{q}_1 - \mathbf{q}_2}{2}\ , \\ \mathbf{P} &= \mathbf{p}_1 + \mathbf{p}_2 \quad , \quad \mathbf{p} = \frac{\mathbf{p}_1 - \mathbf{p}_2}{2}\ .\end{aligned} \tag{5.42}$$

We thus find

$$\begin{aligned}&\langle \mathbf{p}_1 s_1 t_1, \mathbf{p}_2 s_2 t_2|J^\nu|\mathbf{k}_1\sigma_1\tau_1, \mathbf{k}_2\sigma_2\tau_2\rangle = \int d^3X d^3x e^{-i\mathbf{P}\cdot\mathbf{X}}e^{-i\mathbf{p}\cdot\mathbf{x}}\int\frac{d^3Q}{(2\pi)^3}\frac{d^3\xi}{(2\pi)^3}e^{-i\mathbf{Q}\cdot\mathbf{X}}e^{i\boldsymbol{\xi}\cdot\mathbf{x}}e^{i\mathbf{k}\cdot\mathbf{x}} \\ &\times \bar{u}_{s_1}\Big(\frac{\mathbf{P}}{2}+\mathbf{p}\Big)\bar{u}_{s_2}\Big(\frac{\mathbf{P}}{2}-\mathbf{p}\Big)\chi^+_{t_1}\chi^+_{t_2}J^\mu\Big(\frac{\mathbf{Q}}{2}+\xi, \frac{\mathbf{Q}}{2}-\xi\Big)\chi_{\tau_1}\chi_{\tau_2}u_{\sigma_1}(\mathbf{k})u_{\sigma_2}(-\mathbf{k}) \\ &= \bar{u}_{s_1}\Big(\frac{\mathbf{P}}{2}+\mathbf{p}\Big)\bar{u}_{s_2}\Big(\frac{\mathbf{P}}{2}-\mathbf{p}\Big)\chi^+_{t_1}\chi^+_{t_2}J^\nu\Big[\frac{\mathbf{P}}{2}+(\mathbf{p}-\mathbf{k}), \frac{\mathbf{P}}{2}-(\mathbf{p}-\mathbf{k})\Big]\chi_{\tau_1}\chi_{\tau_2}u_{\tau_1}(\mathbf{k})u_{\tau_2}(-\mathbf{k})\ ,\end{aligned} \tag{5.43}$$

where $u_s(\boldsymbol{p})$ and χ_s denote Dirac and Pauli spinors, respectively. Note that, although the electromagnetic current is diagonal in isospin space, we have kept the isospin dependence of matrix elements explicit, for future use in the case of the charged weak current.

Collecting things together we finally arrive at

$$\begin{aligned}\langle \mathbf{p}_1 s_1 t_1, \mathbf{p}_2 s_2 t_2 | J^\nu | \mathbf{k}_1 \sigma_1 \tau_1, \mathbf{k}_2 \sigma_2 \tau_2 \rangle = \int \frac{d^3k}{(2\pi)^3} \Big(\frac{m}{E_k}\Big) \tilde{\psi}(k) \\ \times \langle J_1^\nu \Big[\frac{\mathbf{P}}{2} + (\mathbf{p} - \mathbf{k})\Big] (2\pi)^3 \delta^{(3)} \Big[\frac{\mathbf{P}}{2} - (\mathbf{p} - \mathbf{k})\Big] + J_1^\nu \Big[\frac{\mathbf{P}}{2} - (\mathbf{p} - \mathbf{k})\Big] (2\pi)^3 \delta^{(3)} \Big[\frac{\mathbf{P}}{2} + (\mathbf{p} - \mathbf{k})\Big] \\ + J_2^\nu \Big[\frac{\mathbf{P}}{2} + (\mathbf{p} - \mathbf{k}), \frac{\mathbf{P}}{2} - (\mathbf{p} - \mathbf{k})\Big] \rangle \end{aligned} \tag{5.44}$$

where $\langle \dots \rangle$ denotes the spin-isospin matrix element, summed over $\sigma_1, \sigma_2, \tau_1$ and τ_2.

The resulting expression of the target tensor

$$\begin{aligned} W^{\mu\nu} = & \frac{1}{3} \sum_M \sum_{s_1 s_2} \sum_{t_1 t_2} \int \frac{d^3P}{(2\pi)^3} \frac{d^3p}{(2\pi)^3} \delta[\omega + M - E_X(\mathbf{P}, \mathbf{p})] \delta^{(3)}(\mathbf{q} - \mathbf{P}) \\ & \int \frac{d^3k}{(2\pi)^3} \frac{d^3k'}{(2\pi)^3} \Big(\frac{m}{E_k}\Big) \Big(\frac{m}{E_{k'}}\Big) \tilde{\psi}^*(k') \tilde{\psi}(k) \\ & \langle J_1^\mu(\dots) (2\pi)^3 \delta^{(3)} \Big[\frac{\mathbf{P}}{2} + (\mathbf{p} - \mathbf{k}')\Big] + J_1^\mu(\dots) (2\pi)^3 \delta^{(3)} \Big[\frac{\mathbf{P}}{2} + (\mathbf{p} - \mathbf{k}')\Big] + J_2^\mu(\dots) \\ & \times \langle \mu \to \nu, k' \to k \rangle \ , \end{aligned} \tag{5.45}$$

can be used to obtain the inclusive cross section from Eq. (3.37).

Note that, in the absence of two-nucleon currents the resulting cross section reduces to the form of Eq. (3.53), in which the elementary neutrino cross section is replaced by the corresponding electron cross section and the target spectral function reduces to

$$P(p, E) = |\psi(k)|^2 \delta(E - E_d) \ , \tag{5.46}$$

$E_d = 2.225$ MeV being the deuteron binding energy.

5.4 Numerical results

As a first step, we have tested the approach described in the previous Section including only the one-body current contribution. The current has been constructed following the procedure described in Appendix A, using the state-of-the-art parametrization of the vector form factors of Ref. [13].

The structure of the deuteron wave function employed in all calculations, corresponding to the NN potential model generally referred to as *Argonne* v_{18} [29], is discussed in Appendix C.

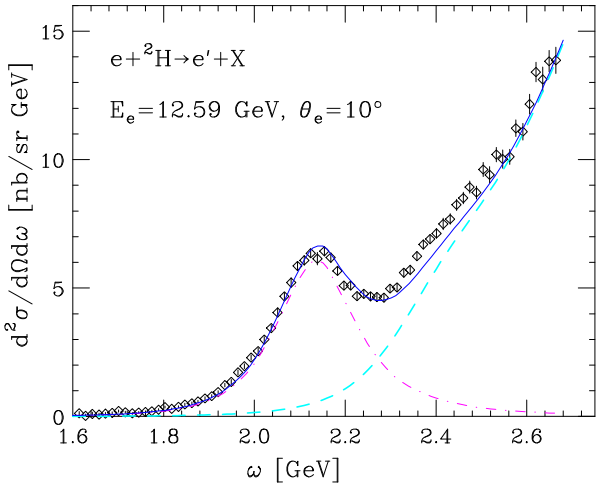

Figure 5.3: Electron-deuteron cross section at beam energy $E_e = 12.59$ GeV and scattering angle $\theta_e = 10°$. The dot-dash and dashed lines correspond to quasi-elastic and inelastic scatering, respectively, whereas the solid lines show the sum of the two contributions. Experimental data are from Ref. [30].

In Fig. 5.3 the results of our calculations are compared to the data of Ref. [30], corresponding to beam energy $E_e = 12.59$ GeV and scattering angle $\theta_e = 10°$. In addition to quasi elastic scattering (dash-dot line), we have included the contributions of single nucleon knockout processes leading to the production of hadrons other than nucleons, as well as deep inelastic scattering, computed within the approach described in Ref.

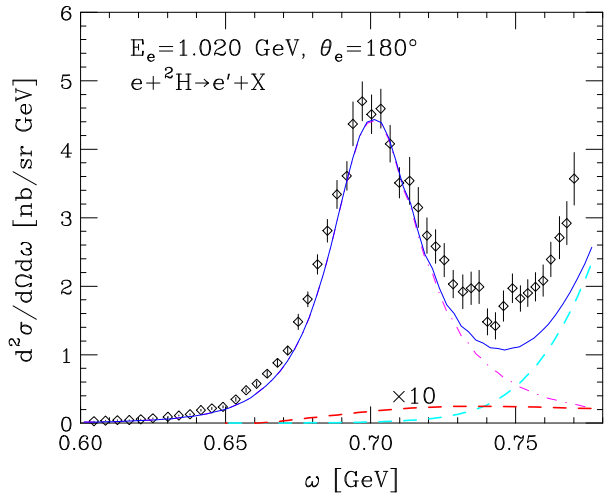

Figure 5.4: Electron-deuteron cross section at beam energy $E_e = 1.020$ GeV and scattering angle $\theta_e = 180°$. The dot-dash and dashed lines correspond to quasi-elastic and inelastic scatering, respectively, whereas the solid lines show the sum of the two contributions. The thick dashed line corresponds to the MEC contribution, multiplied by a factor of 10. Experimental data are from Ref. [31].

[2] (dashed line). It is apparent that the resulting cross section (solid line) provides a quantitative description of the data over the whole range of energy loss, thus suggesting that two-nucleon currents do not play a significant role in this kinematical setup. This was to be expected, as MEC contribute to the cross section in the transverse channel, the contribution of which is strongly suppressed at small scattering angles.

For comparison, in Fig. 5.4 we compare our results to data corresponding to lower electron energy, $E_e = 1.020$ GeV, and backward angle $\theta_e = 180°$ [31]. It clearly appears that in this case the cross section computed including one-body currents only fails to explain the data. Sizable differences between theory and experiment occur in the so called *dip* region, between the quasi elastic peak and the region where inelastic processes dominate. Inclusion of the pion in flight and seagull contributions to the two-nucleon current, described in the previous Section, provides a correction depicted by the thick

dashed line of Fig. 5.4. Note that, to make the MEC contribution visible on the scale of the figure, it has been multiplied by a factor of 10. In the kinematical setup of Fig. 5.3 the calculated MEC contribution turns out to be totally negligible.

The results of Fig. 5.4 indicate that, while the calculated MEC contribution exhibits the expected ω-dependence, it provides a small correction, its magnitude being less than 3% of the cross section obtained from the one-body current. This results strongly suggests that the calculation must be extended to include the full two-body current, taking into account gauge invariance.

Summary and Conclusions

In this Thesis, we have studied the possible role of reaction mechanisms other than single nucleon knock out in the determination of the charged current quasi elastic (CCQE) neutrino-nucleus cross section.

As neutrino oscillation experiments use nuclei as detectors, a fully quantitative understanding of neutrino-nucleus interactions is required to reduce the systematic errors. In this context, the CCQE channel, being dominant at neutrino energies $\lesssim 1$ GeV, is critical to the analysis of the data recently reported by the MiniBooNE Collaboration. Theoretical and experimental studies of electron scattering have shown that the quasi elastic nuclear cross section can be computed to remarkable accuracy within the approach based on the impulse approximation (IA) and Nuclear Many Body Theory (NMBT). In addition to being relevant for data analysis, the study of CCQE neutrino interactions is interesting in its own right, as it may help to clarify the controversial issue of wether the nucleon axial mass, driving the Q^2-dependence of the axial form factor, is modified in the nuclear environment. This possibility has been recently suggested to explain the excess of CCQE events detected by the MiniBooNE and K2K Collaborations using carbon and oxygen targets, respectively. A sizable modification of the axial form factor would be somewhat surprising, as no evidence of a similar effect in the vector form factors has been observed by electron-nucleus scattering. Moreover, the analysis of the sample of CCQE events collected by the NOMAD collaboration using a carbon target does not appear to support a large value of the axial mass.

Based on previous work, we have argued that the excess CCQE cross section is likely to be ascribed to flux average, on account of which in neutrino scattering the contributions of different reaction mechanisms, some of them leading to the same final state, mix up. Of particular relevance, in this context, are the contributions of processes involving meson-exchange currents (MEC), which is known to be sizable in the electron-nucleus scattering cross section in the transverse channel.

As a first step towards the development of a consistent treatment of one- and two-nucleon currents, we have considered the contribution of pion-exchange currents in the case of electron-deuteron scattering. Our numerical results suggest that these contributions are negligible at small angle, where the data can be explained in terms of ons-body current only. At backward angles, while not be totally negligible, the calculated MEC contribution turns out to be small, and does not explain the discrepancy between theory and data.

Numerical calculations have required the development of new computer code in fortran language, as well as significant revisions of the existing code. The typical CPU time needed to compute the total CCQE cross section at fixed neutrino energy turned out to be of the order of few minutes on a high level personal computer.

The work described in the Thesis must be regarded as part of an ongoing effort, aimed at extending the formalism successfully applied to the analysis of electron-scattering data to the case of neutrino scattering. This approach has already produced high quality results for the single nucleon knock out contribution to the CCQE neutrino-nucleus cross section, allowing at the same time for the identification of the problems arising from the flux average that led us to investigate the role of competing reaction mechanisms..

Further development of our project will require the inclusion of exchange currents associated with mesons other than pions, and a careful treatment of the problem of gauge invariance, needed to achieve consistency between the two-body current and the nuclear hamiltonian employed in the calculation of the nuclear spectral functions. The final goal

is the calculation of the neutrino-carbon cross section using one- and two-nucleon vector and axial currents.

Appendix A

Form factors

A.1 Nucleon current

The hadronic currents are not easily expressed in terms of quarks currents because of the composite structure of the hadrons, but the hadronic currents must obey the same fundamental symmetries as the quark currents. The hadronic currents should then have the V-A structure of (vector current) - (axial current).

$$\langle \mathbf{p}' | j^{+}_{had\mu} | \mathbf{p} \rangle = j^{V}_{\mu} - j^{A}_{\mu} \tag{A.1}$$

As the Lorentz vectors, the vector and axial currents are written as

$$j^{V}_{\mu} = \bar{u}(\mathbf{p}') \Big[\gamma_{\mu} F_V(q) + \frac{i\sigma^{\mu\nu} q^{\nu}}{2M} + q_{\mu} F_S(q) \Big] u(\mathbf{p}) \tag{A.2}$$

$$j^{A}_{\nu} = \bar{u}(\mathbf{p}) \Big[\gamma_{\mu}\gamma_5 F_A(q) + \gamma_5 q_{\mu} F_P(q) + i\gamma_5 \sigma_{\mu\nu} q^{\nu} F_T(q) \Big] u(\mathbf{p}) \tag{A.3}$$

Here, u's are the nucleon spinors. When nucleon currents are assumed to be transferred in the same way as the quark current under the charge conjugation and time reverse, the second-class form factors, $F_T(q)$ and $F_S(q)$, vanish and all other form factors become real.

A.2 Nucleon form factors

The weak (charge-lowering) current, $p \to n$ and its conjugate $n \to p$, together with the electromagnetic current, are believed to form an isospin triplet of conserved vector currents. The form factors in the weak current are then directly related to those in the electromagnetic current. The weak-charged current is the incremental or decremental operator of isospin, that is, the current is expressed by the components (τ_1 and τ_2) of the isovector, i.e.

$$J_\mu^\pm = \bar{U}\Gamma_\mu \frac{\tau_1 \pm \tau_2}{2} U \tag{A.4}$$

where $\Gamma_\mu = \gamma_\mu F_V(q) + i\sigma_{\mu\nu}q^\nu F_M(q)/(2M)$ and U is the isodublet, $(p \quad n)^T$. On the other hand, the electromagnetic current is the sum of the isoscalar and the diagonal component (τ_3) of the isovector and then

$$J_\mu^{em} = \frac{1}{2}\bar{U}\Gamma_\mu^S U + \bar{U}\Gamma_\mu \frac{\tau_3}{2} U \tag{A.5}$$

The first term in the right-hand side of the above equation is the isoscalar current and the other is the isovector current. Decomposing the above equation into the proton and neutron currents, we obtain

$$J_\mu^{em} = \bar{p}\frac{1}{2}\Big(\Gamma_\mu^S + \Gamma_\mu\Big)p + \bar{n}\frac{1}{2}(\Gamma_\mu^S - \Gamma_\mu)n \tag{A.6}$$

Therefore the form factors of the isovector current becomes

$$F_i(q) = F_i^p(q) - F_i^n(q) \tag{A.7}$$

The form factors in the vector current, $F_V(q)$ and $F_M(q)$ are determined phenomenologically as:

$$F_V(q) = \left(1 - \frac{q^2}{4M^2}\right)^{-1}\left[G_E(q) - \frac{q^2}{4M^2}G_M(q)\right] \tag{A.8}$$

$$F_M(q) = \left(1 - \frac{q^2}{4M^2}\right)^{-1}\left[-G_E(q) + G_M(q)\right] \tag{A.9}$$

Here, $G_E(q)$ and $G_M(q)$ are Sachs form factors,

$$G_E^p(q) = \frac{G_M^p(q)}{\mu_p} = \frac{G_M^n(q)}{\mu_n} = \left(1 - \frac{q^2}{M_V^2}\right)^{-2} \tag{A.10}$$

and $G_E^n(q) = 0$, where the subscripts p and n denote the form factors for the proton and neutron, respectively. The size parameter is taken to be $M_V^2 = 0.71$ GeV^2. The proton and neutron magnetic moments are $\mu_p \approx 2.793$ and $\mu_n \approx -1.913$ in the unit of the nuclear magneton ($e\hbar/2M_p$ with M_p, the proton mass). We thus obtain the Sachs form factors for the charged current as

$$G_E(q) = \left(1 - \frac{q^2}{M_V^2}\right)^{-2} \tag{A.11}$$

$$G_M(q) = (\mu_p - \mu_n)\left(1 - \frac{q^2}{M_V^2}\right)^{-2} \tag{A.12}$$

The form factors in the axial current, namely, $F_A(q)$ and $F_P(q)$, are related as

$$F_p(q) = \frac{2MF_A(q)}{m_\pi^2 - q^2} \tag{A.13}$$

under PCAC (partially conserved axial current) hypothesis

$$\partial^\mu j_\mu^{Aa} = f_\pi m_\pi^2 \pi^a \tag{A.14}$$

with (a= 1, 2, and 3) together with the assumption that the gauge bosons couple with the nucleon dominantly through the pion exchange in the pseudoscalar channel. $F_A(q)$ is

phenomenologically determined as

$$F_A(q) = g_A \left(1 - \frac{q^2}{M_A^2}\right)^{-2} \tag{A.15}$$

with

$$\begin{aligned} g_A &= -1.261 \pm 0.004 \\ M_A &= 1.032 \pm 0.036 \end{aligned} \tag{A.16}$$

The $F_P(q)$ contribution can be neglected except for the case of the tau-neutrino cross sections.

A.3 Comments

The vector current associated with the nucleon in free space, is conserved, as

$$\begin{aligned} q^\mu j_\mu^V &= \bar{u}(\mathbf{p}') \Big[q^\mu \gamma_\mu F_V(q) + \frac{i\sigma_{\mu\nu} q^\mu q^\nu}{2M} F_M(q) \Big] u(\mathbf{p}) \\ &= \bar{u}(\mathbf{p}') [(p'^\mu \gamma_\mu - p^\mu \gamma_\mu) F_V(q)] u(\mathbf{p}) \\ &= 0 \end{aligned} \tag{A.17}$$

where we used $\sigma_{\mu\nu} = -\sigma_{\nu\mu}$ and the Dirac equation for the nucleon free-space

$$p^\mu \gamma_\mu u(\mathbf{p}) = M u(\mathbf{p}) \tag{A.18}$$

This Dirac equation is not valid for the interacting nucleon, such as nucleons in nuclei. The vector current is not conserved when the nucleus is described by a system of the interacting nucleons through static potentials. The conservation can be recovered by properly including the meson degrees of freedom, such as the exchange currents.

As well known, the axial current is not conserved in free space:

$$\begin{aligned} q^\mu j_\mu^A &= \bar{u}(\mathbf{p}') \big[q^\mu \gamma_\mu \gamma_5 F_A(q) + q^2 \gamma_5 F_P(q) \Big] u(\mathbf{p}) \\ &= \bar{u}(\mathbf{p}') \big[i\sqrt{2} f_\pi(q^2) m_\pi^2 \pi^{(-)} \Big] u(\mathbf{p}) \\ &= \frac{2 f_\pi(m_\pi)^2 m_\pi^2}{q^2 - m_\pi^2} g_{\pi NN}(q^2) \bar{u}(\mathbf{p}') \gamma_5 u(\mathbf{p}) \end{aligned} \tag{A.19}$$

where the PCAC hypothesis is applied as an operator relation with $\pi^{(-)} = (\pi_1 - i\pi_2)/\sqrt{2}$.

Appendix B

Integration limits

Let us analyze in detail the integration limits involved in the calculation of the quasi-elastic and anelastic cross sections. The integration over momentum in neutrino-nucleus cross section can be cast in the form

$$d^3p = p^2 dp d\cos\gamma d\phi \tag{B.1}$$

where γ is the angle between $\mathbf{p}$ and $\mathbf{q}$ and the integral on the azimuthal angle ϕ can be readily done, yielding a factor 2π. Denoting by W the invariant mass of the final hadronic state produced in the interaction, $\cos\gamma$ can be written in the form:

$$\cos\gamma = \frac{-W^2 - |\mathbf{p}|^2 - |\mathbf{q}|^2 + (\tilde{\omega} + E_p)^2}{2|\mathbf{p}||\mathbf{q}|} \tag{B.2}$$

or, equivalently,

$$\cos\gamma = \frac{s + M_{A-1}^2 - W^2 - 2(\omega + M_A)E_{A-1}}{2|\mathbf{p}||\mathbf{q}|} \tag{B.3}$$

where $M_{A-1} = M_A - M + E$, s is the squared center of mass energy and $E_{A-1}^2 = M_{A-1}^2 + |\mathbf{p}|^2$. The quantity $\cos\gamma$ has to satisfy the constraint $-1 \leq \cos\gamma \leq 1$, leading to the lower and upper bounds for $|\mathbf{p}|$:

$$|\mathbf{p}|^{\pm} = \frac{1}{2s}\Big|\Lambda|\mathbf{q}| \pm (\omega + M_A)[\Lambda^2 - 4sM_{A-1}^2]^{1/2}\Big| \tag{B.4}$$

with $\Lambda = s + M_{A-1}^2 - W^2$. The upper limit of the E integration can be found requiring the argument of the square root entering the definition of $|\mathbf{p}|^{\pm}$ to be non negative. This

leads to $\Lambda \geq 2\sqrt{s}M_{A-1}$ and finally to the bound

$$E_{max} = \sqrt{s} - M_A - (W - M) \tag{B.5}$$

We restrict ourselves to the quasi-elastic case. Up to now the integration limits we have found are completely general. The quasi-elastic case is recovered once we put $W = M$. The $\nu - nucleus$ cross section can be cast in a simpler form once we use the energy conserving δ-function to perform integration on $\cos\gamma$ in Eq. (B.1).

We have to evaluate the Jacobian of the transformation

$$\frac{\partial}{\partial \cos\gamma}(s - M^2) \equiv 2|\mathbf{p}||\mathbf{q}|, \tag{B.6}$$

leading to the final formula

$$\frac{d^2\sigma_{IA}}{d\Omega dE_l} = \frac{2\pi}{|\mathbf{q}|}\int dpdE|\mathbf{p}|P(\mathbf{p},E)\frac{d^2\sigma_{elem}}{d\Omega dE_l} \tag{B.7}$$

The integration limits of the Resonance production case are analyzed in Ref[[**?**]].

Appendix C

Deuteron wave function

The general form of the deuteron wave fuction is given by:

$$\psi(\mathbf{r}_1, \mathbf{r}_2) = \Omega^{-1/2} e^{i\mathbf{P}\cdot\mathbf{R}} \psi(\mathbf{r}) \tag{C.1}$$

in which center of mass and relative coordinates (both in position and impulse basis), namely

$$\begin{aligned} \mathbf{R} &= \frac{(\mathbf{r}_1 + \mathbf{r}_2)}{2} \\ \mathbf{r} &= \mathbf{r}_1 - \mathbf{r}_2 \\ \mathbf{P} &= \mathbf{p}_1 + \mathbf{p}_2 \\ \mathbf{p} &= \frac{\mathbf{p}_1 - \mathbf{p}_2}{2} \end{aligned} \tag{C.2}$$

have been introduced. Therefore, the probability of finding the two nucleons with relative distance $\mathbf{r}$ is:

$$\left|\psi(\mathbf{r})\right|^2 \tag{C.3}$$

let us try to formally derive its expression.

The deuteron is the only bound state of two nucleons, with isospin T= 0, spin parity $J^\pi = 1^+$, and binding energy $E_B = 2.225$ MeV. For two-spin 1/2 nucleons, only total spins S= 0, 1 are allowed. Then the total orbital angular momentum is restricted to $J - 1 < l < J + 1$, i.e. l= 0,1 or 2. Since the parity is $\pi = (-1)^l = +1$, only l= 0 and l=

2 are allowed, this also implies we have S= 1.

We begin combining the two spins together to produce a total spin S= 1.

$$\chi_1^1 = |\uparrow_1\rangle|\uparrow_2\rangle \tag{C.4}$$

$$\chi_1^0 = \sqrt{\frac{1}{2}}\Big(|\uparrow_1\rangle|\downarrow_2\rangle + |\downarrow_1\rangle|\uparrow_2\rangle\Big) \tag{C.5}$$

$$\chi_1^{-1} = |\downarrow_1\rangle|\downarrow_2\rangle \tag{C.6}$$

Recalling the following definitions:

$$Y_{0,0} = \frac{1}{\sqrt{4\pi}} \tag{C.7}$$

$$Y_{1,1} = -\sqrt{\frac{3}{8\pi}}e^{i\phi}\sin\theta \qquad , \qquad Y_{1,0} = \sqrt{\frac{3}{4\pi}}\cos\theta \tag{C.8}$$

$$Y_{2,2} = \sqrt{\frac{15}{32\pi}}e^{i2\phi}\sin^2\theta, \quad Y_{2,1} = -\sqrt{\frac{15}{32\pi}}e^{i\phi}\sin 2\theta, \quad Y_{2,0} = \sqrt{\frac{5}{16\pi}}(3\cos^2\theta - 1) \tag{C.9}$$

$$\tag{C.10}$$

we define the spin angle functions, i.e. $\mathscr{Y}$ as:

$$\mathscr{Y}_{lsj}^{m_j} = \sum_{m_s}\langle l, s; m_l, m_s|jm_j\rangle\chi_s^{m_s}Y_l^{m_l} \tag{C.11}$$

where:

$$\langle l, s; m_l, m_s|jm_j\rangle \tag{C.12}$$

is the Clebsh-Gordon coefficient. As an example:

$$\begin{aligned}\mathscr{Y}_{001}^1(\hat{r}) &= \sum_{m_s}\langle 0,1;0,m_s|0,1\rangle\chi_1^{m_s}Y_0^0(\hat{r}) \\ &= \langle 0,1;0,1|0,1\rangle\chi_1^1Y_0^0(\hat{r}) \\ &= \chi_1^1Y_0^0(\hat{r})\end{aligned} \tag{C.13}$$

Thus, the deuteron wave function depending on the relative coordinate, is written as:

$$\psi(\mathbf{r}) = \frac{u(r)}{r}\mathscr{Y}_{011}^1(\hat{r}) + \frac{w(r)}{r}\mathscr{Y}_{211}^1(\hat{r}) \tag{C.14}$$

yielding to:

$$|\psi(\mathbf{r})|^2 = \frac{1}{4\pi}\frac{u^2(r)}{r^2} + \frac{1}{32\pi}\frac{w^2(r)}{r^2}\Big[(3\cos^2\theta - 1)^2 + 18\cos^2\theta\cdot\sin^2\theta + 9\sin^4\theta\Big] + \frac{1}{4\pi}\frac{1}{\sqrt{2}}\frac{u(r)w(r)}{r^2}(3\cos^2\theta - 1) \tag{C.15}$$

$u(r)$ and $w(r)$ indicate the radial functions, moreover $\mathscr{Y}$'s are normalized so that the functions obey the condition:

$$\int_0^\infty dr\big\{u^2(r) + w^2(r)\big\} = 1 \tag{C.16}$$

If the neutron-proton potential is:

$$V(\mathbf{r}) = V_c(\mathbf{r}) + V_T(\mathbf{r})S_{12} + V_{LS}\mathbf{L}\cdot\mathbf{S}, \tag{C.17}$$

where

$$S_{12} = 3(\sigma_1\cdot\mathbf{r})(\sigma_2\cdot\mathbf{r})/r^2 - \sigma_1\cdot\sigma_2, \tag{C.18}$$

then the equations for $u(r)$ and $v(r)$ are:

$$\begin{aligned}\frac{d^2u}{dr^2} &= \{-\epsilon + f_1(r)\}u + f_2(r)w\\ \frac{d^2w}{dr^2} &= f_2(r)u + \{-\epsilon + \frac{6}{r^2} + f_2(r)\}w,\end{aligned} \tag{C.19}$$

where

$$\epsilon = ME/\hbar^2 \tag{C.20}$$

and

$$\begin{aligned}f_1(r) = MV_c(r)/\hbar^2, \quad f_2(r) = 8^{1/2}MV_T(r)/\hbar^2,\\ f_3(r) = M\big[V_c(r) - 2V_T(r) - 3V_{LS}(r)\big]/\hbar^2\end{aligned} \tag{C.21}$$

The boundary conditions are that $u = w = 0$ for $r = 0$ and for $r \to \infty$.

Bibliography

[1] Proceedings of NUINT11 (Dehradun, India, March 2011). AIP Conference Proceedings, Vol. 1405 (2011).

[2] O. Benhar, D. Day, and I. Sick, Rev. Mod. Phys **80**, 189 (2008).

[3] E. Majorana, Nuovo Cimento **14**, 171 (1937).

[4] G. Altarelli, F. Feruglio, arXiv:/0405048v2 [hep-ph].

[5] F.P. An *et al* (Daya Bay Collaboration), Phys. Rev. Lett. **108**, 171803 (2012).

[6] S. Abe *et al* (KamLAND Collaboration), Phys. Rev. Lett. **100**, 221803 (2008).

[7] B. Aharmim *et al* (SNO Collaboration), Phys. Rev. C **72**, 055502 (2005).

[8] P. Fisher, B. Kayser, K.S. McFarland, arXiv:9906244v1 [hep-ph].

[9] A.A. Aguilar-Arevalo *et al.* (MiniBooNE Collaboration), Phys. Rev. D **81**, 092005 (2010).

[10] O. Benhar, P. Coletti, and D. Meloni, Phys. Rev. Lett. **105**, 132301 (2010).

[11] G. C. M. Martini, M. Ericson, and J. Marteau, *Phys Rev. C* **81**, 045502 (2010).

[12] J. Nieves, I. R. Simo, and M. V. Vacas, Phys. Lett. **B707**, 72 (2012).

[13] A. Bodek, S. Avvakumov, R. Bradford, and H. Budd, Eur. Phys .J. C **53**, 349 (2008).

[14] R. Gran *et al.* (K2K Collaboration), Phys. Rev. D **74**, 052002 (2006).

[15] V. Lyubushkin *et al*, Eur. Phys. J. C **63**, 355 (2009).

[16] O. Benhar and D. Meloni, Phys. Rev. D, **80**, 073003 (2009).

[17] O. Benhar, A. Fabrocini, S. Fantoni, & I. Sick, Nucl. Phys. A **579**, 493 (1994).

[18] O. Benhar *et al*, Phys. Rev. D **72**, 053005 (2005).

[19] S.C. Pieper, R.B. Wiringa and V.R. Pandharipande, Phys. Rev. C **46**, 1741 (1992).

[20] J. S. O′Connell *et al Phys Rev. C* **35**, 1063 (1987).

[21] O. Benhar, invited talk at NUFACT11 (Geneva, Switzerland, August 2011), arXiv:1110.1835v1 [hep-ph].

[22] R.M. Sealock *et al* 1989 *Phys Rev. Lett.*, **62** 1350 (1989).

[23] J. Carlson and R. Schiavilla, Rev. Mod. Phys. **70**, 743 (1998).

[24] W.A. Mann *et al*, Phys. Rev. Lett. **31**, 844 (1973).

[25] S.J. Barish *et al*, Phys. Rev. D **16**, 3103 (1977).

[26] N.J. Baker *et al*, Phys. Rev. D **23**,2499 (1981).

[27] D.O. Riska, Phys. Scr. **31**, 107 (1985).

[28] D.O. Riska, Phys. Scr. **31**, 471 (1985).

[29] R.B. Wiringa, V.G.J. Stoks and R. Schiavilla, Phys. Rev. C **51**, 38 (1995).

[30] S. Rock *et al*, Phys. Rev. D **46**, 24 (1992).

[31] R.G. Arnold *et al*, Phys. Rev. Lett. **61**, 806 (1988).